Visiting scientist report within the SAF on climate monitoring

Precipitable Water in Cloudy Area

(VS Plan 7.7)

Heike Hauschildt and Andreas Macke
IFM–GEOMAR
Leibniz Institut für Meereswissenschaften
Düsternbrooker Weg 20
D–24105 Kiel

Contents

Chapter 1

Introduction

The spatial and temporal pattern of atmospheric water vapour describes the current state of our climate system. Water vapour affects the tropospheric temperature due to greenhouse warming stronger than other atmospheric gases. It is the mandatory condition for clouds and the hydrological cycle. The changes in cloud cover control the net warming/cooling processes. The range in estimated climate sensitivity of 1.5 to 4.5° C for a CO_2 doubling is largely dictated by the interaction of model water vapour feedbacks with the variations in cloud behavior among existings models (IPCC Working Group I (2001)).

To understand the role of water vapour in our climate system a realistic monitoring of global water vapour distributions, both horizontally and vertically, is required. Satellite remote sensing offers the possibility to retrieve the vertical structure of the atmosphere under cloud free conditions. The corresponding radiometers operate at infrared wavelengths, so they are not applicable when clouds are inside the radiometer field of view (FOV). Because cloudy skies usually contain more water vapour then cloud free areas an underestimation in the retrieved amount of water vapour occurs, the so-called *nice weather bias*, if cloudy scenes are excluded.

Global patterns of water vapour can only be detected by indirect satellite based observations. Radiosonde measurements offer a more direct and more accurate method for obtaining water vapour profiles, but they are limited to a coarse spacial resolution and ocean areas are excluded. This leads to an underestimation due to the negligence of 70% of the Earth's surface, because the lower atmosphere contains more moisture over ocean than over land areas.

The microwave radiometer techniques offer a capable method of measuring both water vapour path and liquid water path simultaneously. The previous literature study by Wahl et al. (2003) summerises the activities done in this field.

For the present study two types of retrieval schemes are used. The vertically integrated liquid water, denoted as liquid water path (LWP), and the water vapour path (WVP), often termed as total precipitable water (TPW) retrieval algorithm used by NOAA–NESDIS (Grody et al. (2001)) for their product generation is based on a two frequency scheme using a linear regression to relate the measured brightness temperatures to the used frequencies. Brightness

temperatures measured in 23.8 GHz frequency are strongly related to the water vapour content in the atmosphere whereas the 31.4 GHz frequency are the response to the liquid water, see section 2.1.1. The second algorithm is based on a neural network scheme developed at the IFM–GEOMAR. A more detailed describtion is also given in section 2.1.1. A comparison is shown in chapter 3.

For the neural network retrieval the influence of cloud cover inside the field of view (FOV) on the relation between the retrieved LWP and WVP is estimated. The sub–FOV cloud cover results from measurements of the Advanced Very High Resolution Radiometer (AVHRR). The AVHRR instrument is on the same satellite as the AMSU, so no co-location problems due to different orbits occur. The cloud detection scheme is based on a two channel thresholding technique. The method is described in section 2.2. One channel measures the reflected solar radiation, therefore this method is limited to day time overpasses. The overpasses used in this study are over the North Atlantic during May to September 2001. Only one overpass per day has been considered. The results are shown in section 4.1.

For the NOAA–NESDIS retrieval algorithm investigations on global and more climatological scale are performed. Global AMSU measurements for the whole year 2001 are considered. The relation of LWP and WVP is investigated on different time and spatial scales for the three major ocean areas. A special focus is given on the influence of cloud types, see section 4.2.

Within the EU–Project CLIWA-NET three intensive field campaigns were performend to measure cloud properties and to validate satellite LWP algorithms with ground based radiometers. As a result of the first campaign, CNN1, during August and September 2000, Crewell et al. (2002) estimate as a climatological relationship that the WVP in clear sky is 80% of the WVP in cloudy atmospheres. In this study the excess water vapour in cloudy areas is estimated from satellite observations on the global scale. On a $2.5^\circ \times 2.5^\circ$ spatial resolution and monthly means the relationship mentioned in Crewell et al. (2002) is confirmed. However, large scatter in the data occur, even on climatological averages.

The present study ends with conclusions regarding an improved retrieval of water vapour in cloudy areas.

Chapter 2

Data and Algorithms

The NOAA-KLM satellite generation is equiped with various instruments to retrieve the state of the atmosphere and the surface. The big advantage of using instruments on the same satellite is that the co–location in time and space is limited to the scanning properties and not depending on problems due to different orbits. In this study two instruments are used. The Advanced Microwave Sounding Unit (AMSU), a successor of the MSU, which measures the microwave emission in 20 channels. The main purpose of the instrument is to deliver brightness temperatures to be assimilated into numerical weather prediction models. At the same time it is possible to retrieve cloud properties, humidity profiles and surface properties like surface humidity, sea ice cover for clear and cloudy skies.

Another instrument onboard the same satellite is the Advanced Very High Resolution Radiometer (AVHRR). AVHRR measures the radiances in the visible and near infrared spectral range. The new feature of this instrument is a 1.6μm channel. This channel operates during day time and is switched to 3.7μm channel for measurements during night time. The measured reflectance in the 1.6μm channel is related to the effective radius of cloud dropplets in the upper cloud layer.

These two instruments are onboard the NOAA-15, NOAA-16 and NOAA-17 satellites. The status of these satellites and the data quality differs, see table 2.1. It turned out that only data from NOAA-16 are appropriate for an analysis using both instruments. In section 4.1 the influence of the relation LWP – WVP on cloud cover derived from AVHRR measurements inside the AMSU FOV is investigated using near noon overpasses for the periode May to September 2001. For a study of the global statistics of the excess water vapour derived from AMSU measurements only, all overpasses performed from February to December 2001 were analysed.

2.1 AMSU

The Advanced Microwave Sounding Unit (AMSU) is a 20 Channel microwave cross track scanning instrument. The instrument consists of three modules. In table 2.2 the frequencies are listed, in table 2.3 the technical characteristics are shown. For more informations see the

Satellite	Start date	Status
NOAA-15	25.10.1998	Problems starting in summer 2000. AVHRR and AMSU channel instabilities and failures.
NOAA-16	24.01.2001	No problems reported.
NOAA-17	28.06.2003	Failure in different AMSU frequencies used in this study.

Table 2.1: *Satellite status informations. Source: http://www.saa.noaa.gov. For informations on the instruments related to the overpasses see: http://www.noaa.nesdis.gov/poesstatus/index.asp.*

NOAA-KLM Users Guide (1998). AMSU measures the brightness temperatures for 30 field-of-views. The instrument is flying on the NOAA-KLM series.

Module	channel	frequency [GHz]	bandwidth [MHz]	error NeΔT [K]
AMSU-A2	1	23.80	251.02	0.211
	2	31.40	161.20	0.265
AMSU-A1	3	50.30	161.14	0.219
	4	52.80	380.52	0.143
	5	53.59±0.115	168.20	0.148
	6	54.40	380.54	0.154
	7	54.94	380.56	0.132
	8	55.50	310.34	0.141
	9	57.29	310.42	0.236
	10	57.29±0.217	76.58	0.250
	11	57.29±0.322±0.048	35.11	0.280
	12	57.29±0.322±0.022	15.29	0.399
	13	57.29±0.322±0.010	7.39	0.539
	14	57.29±0.322±0.004	2.94	0.914
	15	89.00	1998.98	0.165
AMSU-B	16	89.00	1000.00	0.37
	17	150.00	1000.00	0.84
	18	183.00±7.0	500.00	1.06
	19	183.00±3.0	1000.00	0.70
	20	183.00±1.0	2000.00	0.60

Table 2.2: *AMSU instrument characteristics*

2.1.1 Microwave radiative transfer

The radiation measured in the microwave narrow frequency bands is the sum of the emissions from the atmospheric gases, the surface and the atmospheric water, see figure 2.1. The surface emission (B) is well known over the oceans. Here it depends mainly on the sea surface temperature and the surface wind speed. The ocean gives a cold homogeneous background for

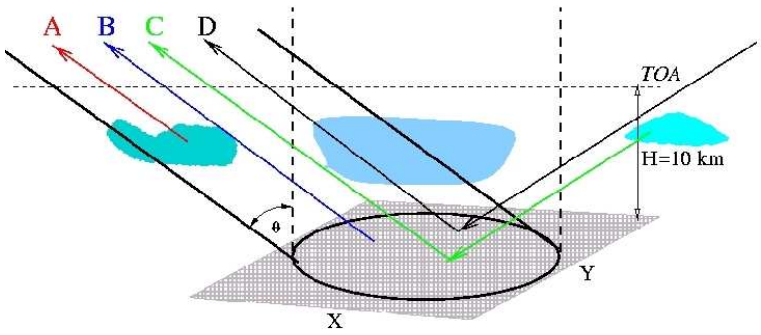

$$
\begin{aligned}
T_B &= T_A(1-\exp(-\delta_A)) \\
&+ (1-\Gamma_r)\,T_S\exp(-\delta_A) \\
&+ \Gamma_r\exp(-\delta_A)T_A(1-\exp(-\delta_A)) \\
&+ \Gamma_r T_{sp}\exp(-2\delta_A)
\end{aligned}
$$

Figure 2.1: *Composition of the microwave signal as measured with a satellite instrument, from* von Bremen et al. *(2002). (A) denotes the atmospheric emission, (B) the surface emission, (C) the reflected atmospheric emission and (D) the reflected background emission. The optical depth of the atmosphere is given by* δ_A.

the atmospheric emission. Over land the surface emission is highly variable. Thus, retrieval of atmospheric parameter using microwave radiances is only suitable, when the background information is homogeneous and well know, like over ocean areas. The variance is in the range of the emission from the atmosphere. The background emission from space (D) is well known. The remaining part is the emission from the atmosphere (A).

In figure 2.2 the transmission as a function of the frequency in the microwave spectra is shown. For the LWP and WVP standard retrieval algorithm two frequencies are used. One near the water vapour absorption line (22.235 GHz), for AMSU it is the 23.4 GHz channel. The second frequency is choosen in the water vapour window, here the 31.4 GHz channel. The first radiance is stronger related to the water vapour in the atmospheric column, the second to the integrated liquid water, see figure 2.3. The signal in both channels is not exclusively related to the water vapour/LWP there is still some influence on the other compound. Therefore, the retrieval of one

	AMSU-A	AMSU-B	AVHRR
scanning direction	cross-track	cross-track	cross-track
viewing angle	3.3°	1.1°	0.0745°
field of view	30	90	2048 LAC 408 GAC
resolution: nadir	50 km	16.3 km	1.1 km LAC 4.km GAC

Table 2.3: *AMSU and AVHRR instrument characteristics.*

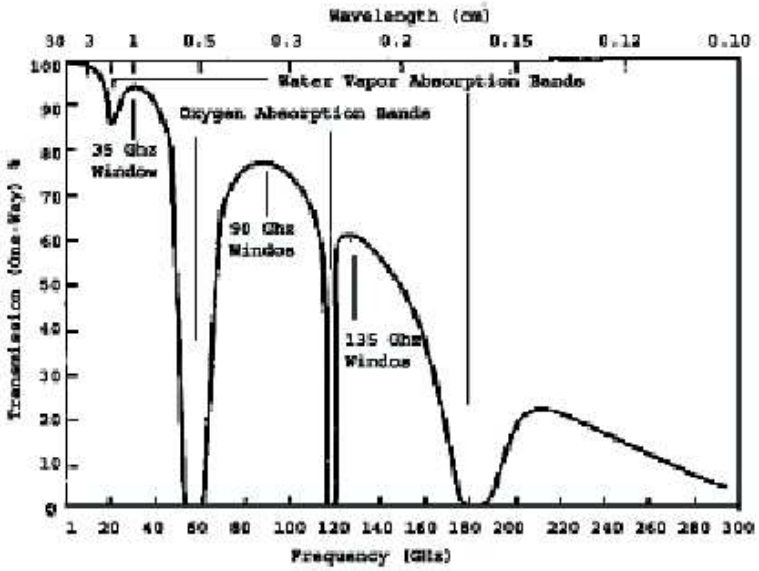

Figure 2.2: *Transmittance as function of the microwave frequency, from* Ulaby et al. *(1981).*

quantity is not independent of the other retrieval.

The NOAA–NESDIS algorithm Grody et al. (2001) is given as:

$$WVP = \cos\left[c_0 + c_1 \ln(T_s - T_B(23.8)) + c_2 \ln(T_s - T_B(31.4))\right] \quad (2.1)$$

$$LWP = \cos\left[d_0 + d_1 \ln(T_s - T_B(23.8)) + d_2 \ln(T_s - T_B(31.4))\right] \quad (2.2)$$

The coefficients c_0 and d_0 are functions of the viewing zenith angle and have been derived from radiative transfer calculations. The algorithm has been validated against SSM/I and radiosonde measurements. The coefficients (c and d) also depend on the wind speed and the used satellite platform (see http://orbit-net.nesdis.noaa.gov). The surface temperature, T_S, defines the radiative background.
The surface informations are taken from the NCEP/NCAR reanalysis data (Kalnay und Coauthors (1996)). For the sea surface temperature (SST) the weekly Reynolds SSTs on a $1.0°\times1.0°$ grid are used. For the wind speed the six hourly reanalysis data on a $2.5°\times2.5°$ grid are used.

From a modeling perspective a known relationship between the radiances and the physical properties of the atmosphere can also be described on a statistical basis. Figure 2.3 shows the correlation between the LWP or WVP and the AMSU brightness temperatures. The non-linearity in the relation can be described with neural network techniques by making use of a large number of ship based radiosonde humidity and temperature profiles to calculate the satellite measured brightness temperature. For the derivation of the neural network algorithm about 8000 radiosonde ascents over the Atlantic ocean and from coastal stations where taken. In

figure 2.4 the positions of the radiosonde ascents are shown. Mainly profiling from the research vessel 'Polarstern' were used (for the Polarstern profiles see KÖNIG-LANGLO UND MARX (1997)). All used profiles exceed the 300 hPa level and ground synoptical observations exist. For the coastal stations an important constraint is, that the wind in the whole profile is off-shore, so the humidity and temperature profile is not influenced by land emission. The adiabatic LWP is calculated from the humidity profiles using the scheme of HARGENS (1992). Microwave radiances have been obtained from the microwave radiative transfer model MWMOD developed by SIMMER (1994). With these data the neural network is trained. The data set is splitted randomly in three parts, two for the training and one for the validation. During the training the neural network cross checks the retrieved algorithm against the results performed with the second data set. The aim is to minimize the cost function but to avoid over training, when the algorithm is not able to retrieve e.g. LWP in an suitable error marge from a new data set. When training and first step validation is done, the third data set is presented to the algorithm. The statistical error, the rms, is now taken as a quality measure for the derived algorithm.

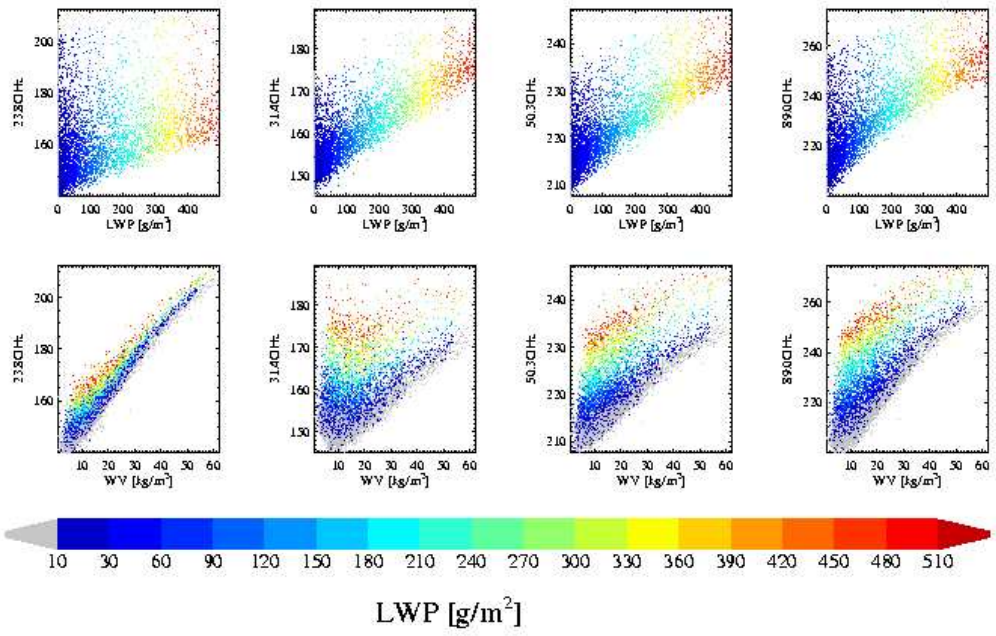

Figure 2.3: *Calculated brightness temperatures at the AMSU channels for a sufficiently large number of atmospheric conditions as a function of LWP and WVP.*

For this study only the brightness temperatures at frequencies 23.8 GHz, 31.4 GHz, 50.3 GHz and 89.0 GHz are used. Figure 2.5 shows the results for the validation data set. The ranked correlation between the modeled WVP and the NN retrieved WVP is 0.99. For the LWP the correlation is 0.87. The neural network is only able to interpolate in the limits defined by the training data set. It is not able to extrapolate. The validation data set is from the brightness temperatures in the limits given by the training data set, but still it is possible, that specific synoptical situations are not included. In figure 2.5 for the WVP a cluster of eight values seem to be not well represented by the neural network, an underestimation occurs. These data points

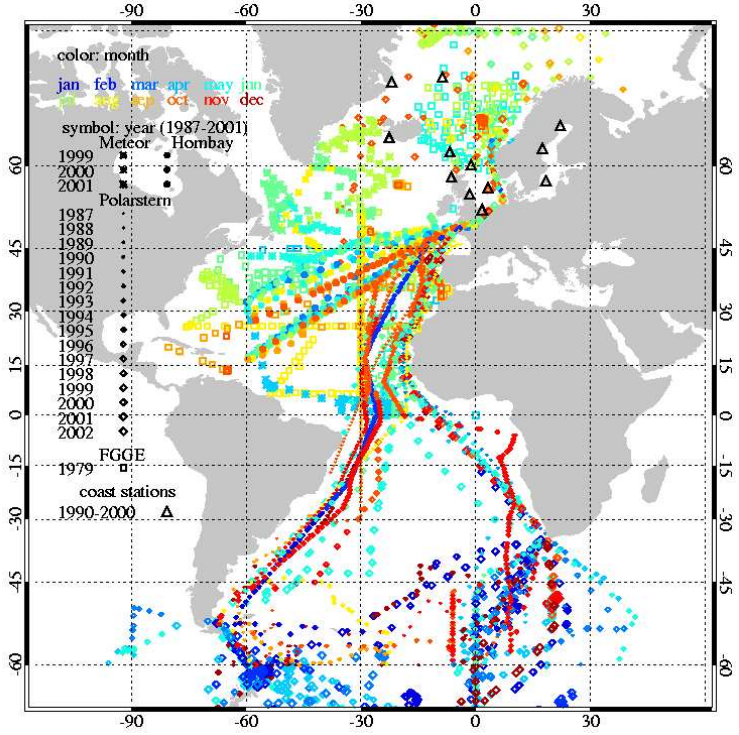

Figure 2.4: *Distribution of the used radiosonde ascents.*

may present such a situation not included in the training data set. This shows the limitations of the neural network technique. Therefore, it is ineluctable to use a comprehensive data set including a wide range of synoptical situations.

Further research shows that the knowledge of surface parameter considerably increases the retrieved accuracy e.g. using the surface temperature as in the NESDIS algorithm.

2.2 AVHRR

The Advanced very high resolution radiometer, AVHRR, measures reflectances in the solar and near infrared spectra, the frequencies are shown in table 2.4, informations on the instrument are in table 2.3. AVHRR is used here for cloud detection purposes on a higher resolution then the AMSU resolution. So the influence of the sub-pixel cloud cover can be estimated. Results are shown in section 4.1.

The AVHRR data are used to estimate the cloud cover inside the AMSU field of view. For the cloud detection a two channel technique is applied. A first thresholding test is done by using the temperature in the 10.4 μm channel. If the pixel has a temperature lower than 273K, clouds are assumed. The second test makes use of the reflectance in the 0.6 μm channel. Here the

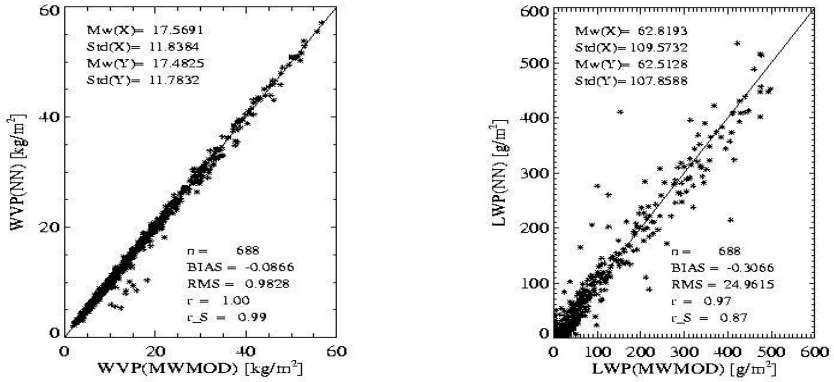

Figure 2.5: *Correlation between NN-retrieved and modelled atmospheric properties. Left: water vapour path, right: liquid water path.*

Channel	1	2	3a	3b	4	5
wavelength [μm]	0.58 - 0.68	0.725- 1.1	1.580- 1.64	3.55 - 3.93	10.3 - 11.3	11.5 - 12.5

Table 2.4: AVHRR channel informations.

pixel must be brighter then a dynamical threshold derived from the whole satellite scene. The distribution of channel 1 reflectances for a scene including clouds over land and sea as well as clear sky land and sea is shown in figure 2.6. Cloud free areas are represented by peaks in the dark end of the distribution, where ocean has a lower albedo as the land. A third peak is in the brighter edge of the distribution which is related to clouds. The dynamical threshold is fixed by the minimum in-between these peaking areas.

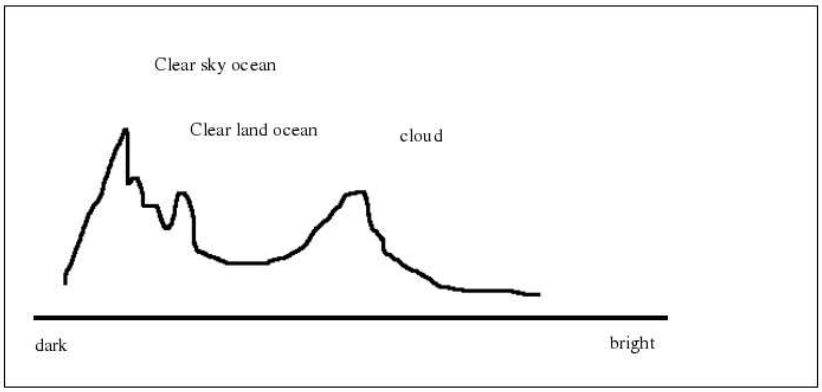

Figure 2.6: *Sketch of a frequency distribution of channel 1 reflectances.*

In a future attempt the cloud dection will be performed with an image processing software, that is aware of the ground conditions. It is planned to use the CM–SAF-Cloud detection scheme for

this purpose.

Chapter 3

Comparison of the two retrieval methods

In order to get an impression about the differences between the results from the statistical neural network scheme and the physically motivated NOAA-NESDIS algorithm, one specific satellite scene is analysed with both methods. Figures 3.1 and 3.2 show the retrieved LWP and WVP field for the NOAA-16 overpass over the North Atlantic from 9. 9. 2001, 14:35 UTC. While the results for the water vapor agree fairly well, large differences occur for the LWP results with a higher variability in the neural network derived fields. These differences are most likely caused by the use of surface informations in the NOAA-NESDIS algorithm. This may stabilize the retrieved atmospheric properties whereas the small-scale atmospheric noise introduces errors in the coupled neural network LWP/WVP retrieval. For the particular scene under consideration the neural network based LWP is larger than the NOAA-NESDIS by a factor of 1.5. This may be caused by the fact that the neural network scheme is trained for LWP smaller than 0.8 kg/m^2 while the NOAA-NESDIS scheme goes up to 2 kg/m^2 and that neural network regressions give unreliable results outside the training area.

Crewell und Löhnert (2003) show that small differences in retrieved LWP and WVP are a result of variations between various absorption models. The mean differences between Liebe (1989) and Liebe et al. (1993) are in the range of 1- 2 K for the lower frequencies, whereas a larger bias for higher frequencies (50, 89 GHz) occurs. The Rosenkranz (1998) gives similar results as Liebe (1989). Some attemps to reduce these uncertainties are made, see Cruz Pol et al. (1998). In this study the Liebe et al. (1993) is used by MWMOD, whereas NOAA/NESDIS uses the Rosenkranz (1998). Nevertheless, the major differences between the neural network and the NOAA-NESDIS algorithms can not be explained by the different absorption schemes.

The neural network based WVP is slightly larger (factor of 6%) compared to the NOAA-NESDIS results, figure 3.3. Although the water vapor retrieval is less sensitive to surface condtions, we suggest the same reasons for the differences as in the discussion of the LWP.

The brightness temperatures in the 23.8 GHz and 31.4 GHz channel are influenced by LWP and

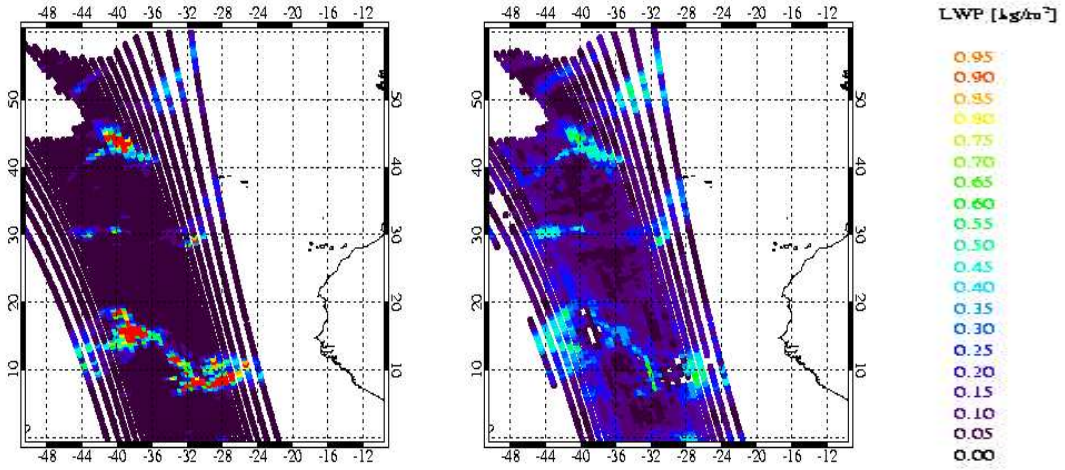

Figure 3.1: *LWP field from 9.9.2001 at 14:35. Left: NOAA-NESDIS, right: neural network. The LWP is given in* kg/m^2.

WVP. In both algorithm these dependencies are not completely seperated. So, it depends on the algorithm wether it tends to derive more LWP or WVP. The neural network and the NOAA NESDIS algorithm have in this aspect different tendencies. The neural network tends to produce higher WVP instead of higher LWP in regions with thick clouds whereas the NOAA NESDIS algorithm obtains higher LWP values over these regions (see figure 3.1 and 3.2., respectively).

For the three reasons explained above (surface information, training range, extrapolationproblems) we conclude to go ahead with the NOAA-NESDIS retrieval scheme within this study except of the cloud cover analysis. Current work is aiming at improving the neural network scheme along these problems. For further studies the cloud retrieval scheme developed in the frame work of the now-casting SAF can be used for analysing the LWP and WVP fields from microwave remote sensing. The advantage is a consistency of all SAF products.

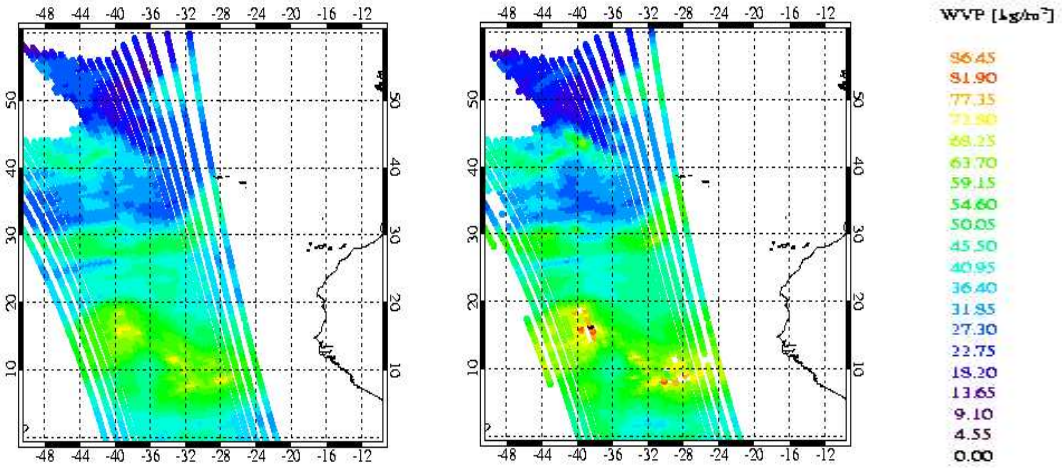

Figure 3.2: *WVP field from 9.9.2001 at 14:35. Left: NOAA-NESDIS, right: neural network. The WVP is given in kg/m^2.*

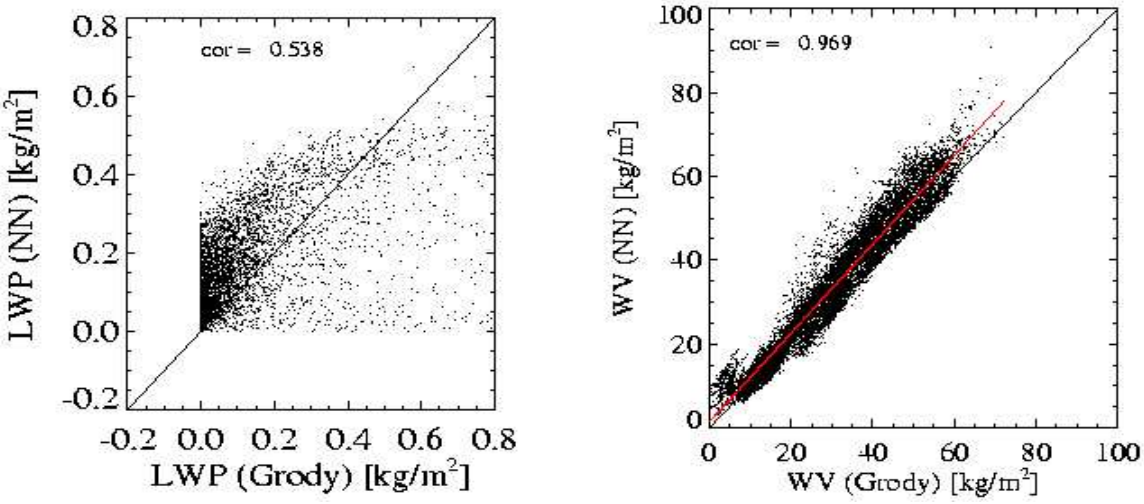

Figure 3.3: *Correlation between NN-retrieved and NOAA-NESDIS atmospheric properties. Left: liquid water path, right: water vapour path. For the water vapour path the regression is given in red.*

Chapter 4

LWP–WVP Relationships

The main purpose of this study is to obtain a link between water vapour in clear and cloudy areas. This information shall be used in future corrections of the nice weather bias. As a first step, the dependency of climatological LWP/WVP relationships will be calculated as a function of cloud cover in section 4.1. The global distribution of water vapour and liquid water is investigated in section 4.2.

4.1 Dependency on cloud cover

AVHRR data for daytime overpasses have been looked at to obtain cloud cover inside an AMSU FOV's. This was done for the North Atlantic region from May 2001 to September 2001. To handle the huge amount of data, only one overpass per day enters the averaging process. The data have been averaged into grid sizes of $1^\circ \times 1^\circ$, $2.5^\circ \times 2.5^\circ$ and $4^\circ \times 4^\circ$ degrees in order to estimate the dependecy of the LWP-WVP relations on averaging scale. Temporal averaging has been performed for the entire time period. Figure 4.1 shows scatterplots of LWP and WVP for the $2.5^\circ \times 2.5^\circ$ degree grid box sizes. Results for the other grid box sizes are given in the appendix B. Not surprisingly, LWP and WVP are positively correlated. No significant changes in the type and degree of the correlation with cloud cover can be inferred. The same is true for the results shown in the appendix.

Obviously, cloud cover alone does not sufficiently distuingish between cases of warm and humid or cold and dry cloudy atmospheres. Further studies are necessary which include improved cloud masks and - more importantly - cloud classification schemes. In the frame work of the CM-SAF cloud properties like cloud cover, cloud phase and cloud type as well as cloud micro physical properties like optical depth, effective radius and LWP are provided. These products can help to investigate the dependency of the relation LWP-WVP on cloud properties.

4.2 Global statistics

As a first step to retrieve the excess water vapour in cloudy atmospheres the frequency distributions of WVP and LWP over ocean areas are examined. Figure 4.2 shows the relative

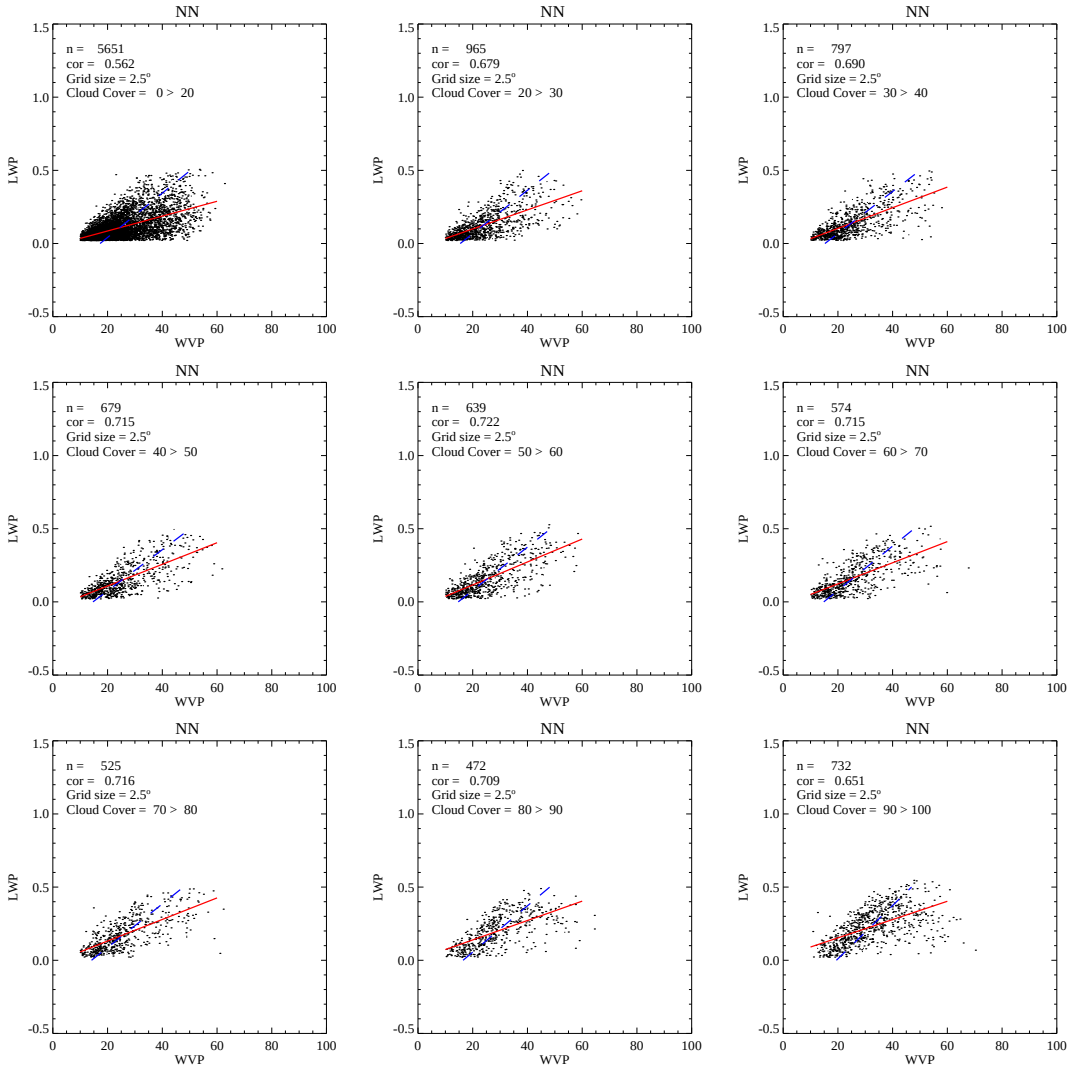

Figure 4.1: *Influence of cloud cover on the relation LWP to WVP. LWP is given in kg/m^2 and the WVP in kg/m^2. The retrieved values are sampled on a 2.5°× 2.5° grid. In red the x-y correlation and in blue the y-x correlation is given.*

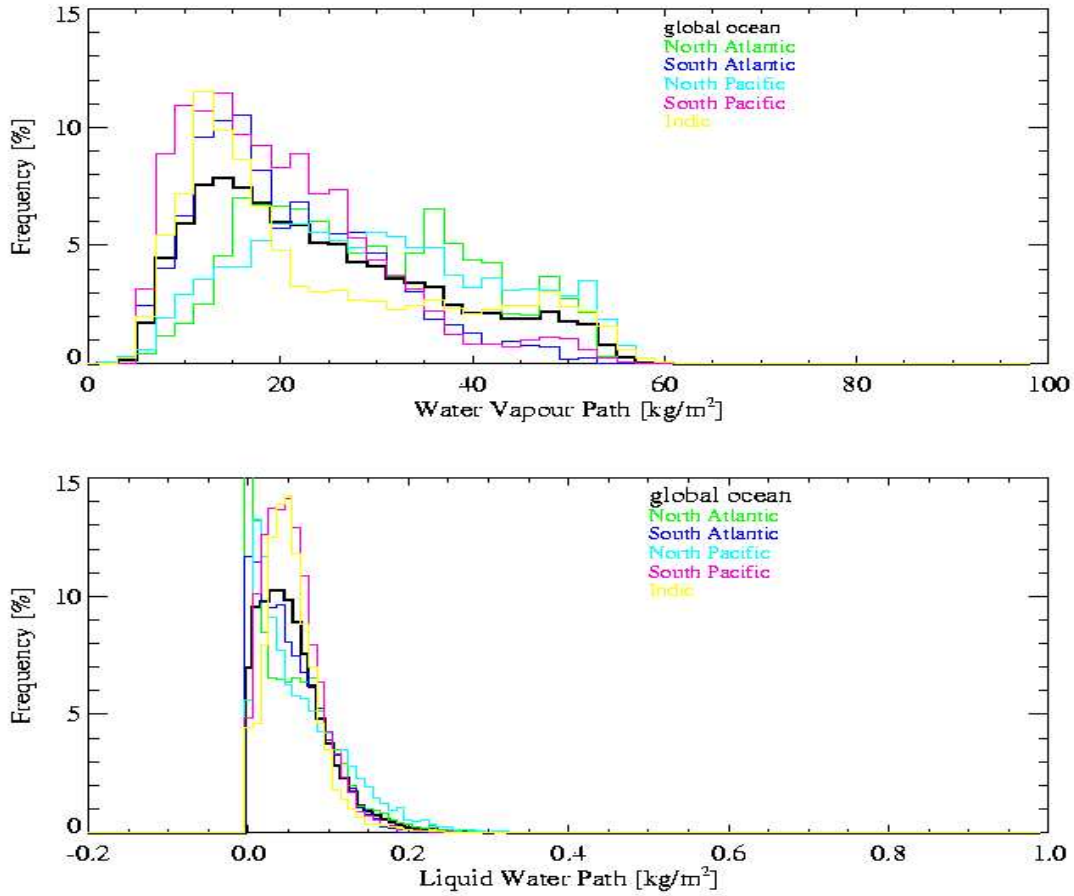

Figure 4.2: Frequency distribution of monthly mean WVP (upper) and LWP (lower) relative to the covered amount of pixels on a 2.5° grid. February to December 2001

occurrence of monthly mean WVP, sampled on a 2.5°, according to the examined amount of grid points. For other spatial and temporal resolutions see Appendix C. The black line describes the global ocean WVP distribution. It resembles a bimodal function with a peak in dry conditions like the mid– to high–latitudes and a second one in the moist air region related to the tropics. A small peak at high values is present in the indic ocean, in the other ocean basins it is not so clearly visible due to the changing position of the inner tropical convergence zone (ITCZ).

The LWP distribution is rather steep and strongly skewed towards smaller values. Similar results have been found for cloud optical thickness distributions from single satellite scene to global scales. The tropical oceans show a tendency towards larger LWPs, forced by strong convection processes. More intense low pressure systems in the Southern Hemisphere may explain the large LWPs.

In figure 4.3 the relation between the WVP and the LWP over the North Atlantic is shown. The whole region is divided into latitude belts. For the Tropics (0-30° latitude) there is no clear

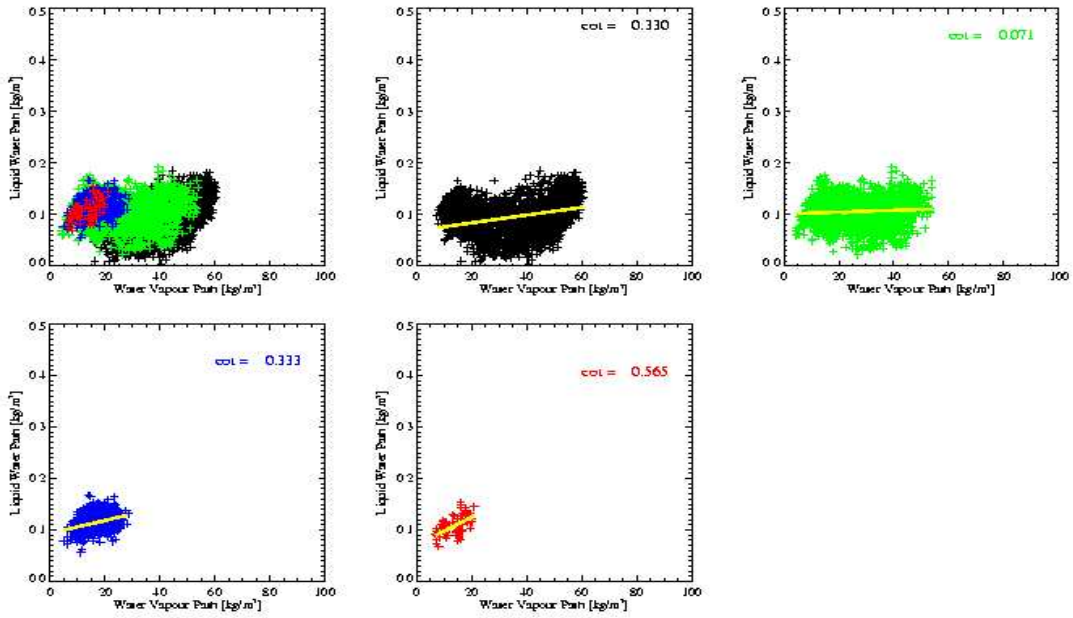

Figure 4.3: *WVP depending on LWP, monthly mean on a 2.5°× 2.5° grid for the North Atlantic. Black: 0-30° North, green: 30-50° North, blue: 50-60° North and red: 60-90° North. The yellow line represents the regression. (February to December 2001).*

correlation. The large cumulonimbus clouds with their ice top and rain water are excluded here, because the large particles reduce the signal in the AMSU channel due to scattering and lower emissions. Therefore, only the clouds with a LWP lower then 0.5 kg/m^2 are taken into account. Again, the relation is not clear. For the subtropics, where shallow cumulus clouds are the dominant feature the relation is not large either. For the mid-latitudes (50-60°) the correlation is getting more significant. The larger stratus cloud fields related to the frontal systems induce the improved correlation. The largest correlation can be found for latitudes higher then 60°.

For the estimation of the excess water vapour in cloudy areas the relation WVP (cloud) and WVP (clear) is calculated. This relation is shown in figure 4.4. The mean excess water vapour factor for the North Atlantic is 1.2. Or inversely taken, the WVP in clear skies is 83% of the WVP in cloudy skies. Crewell et al. (2002) found from ground based measurements in Europe that the WVP in clear sky is 80% of the WVP in cloudy atmospheres. Thus, our global ocean satellite data analysis confirms the experimental findings over land areas that have been obtained from a considerably smaller region and shorter time period (two months). For the Tropics the excess water vapour factor is smaller, the distribution is shown in figure 4.6.

In figure 4.3 a relation between the water vapour path and the LWP is found. For higher WVP the LWP increases, for mid and high latitudes this can be explained by frontal systems which transport stratiform clouds and warm humid air north. Figure 4.4 show that the excess water vapour decreases with increasing WVP in all latitudinal bands. Whereas the excess water vapour increases with increasing LWP, shown in figure 4.5. The slope differs for each latitudinal band.

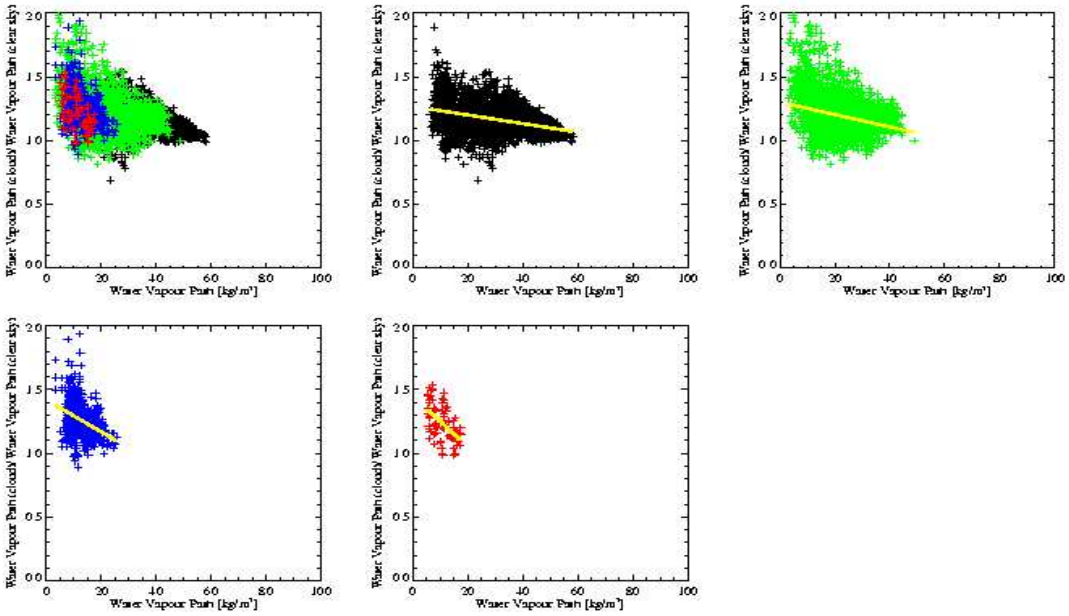

Figure 4.4: *Excess Water Vapour (WVP (cloudy)/WVP (clear)) vs WVP for clear cases, monthly mean on a 2.5°× 2.5° grid for the North Atlantic. Black: 0-30° North, green: 30-50° North, blue: 50-60° North and red: 60-90° North. The yellow line represents the regression. (February to December 2001).*

This relation is prominent in the southern atlantic as well, see Appendix D. The strength of these relations is varying with the season showing highest values during spring and fall. In the mid and high latitudes this can be explained by the higher frequency of low pressure systems. In further studies the relation of the excess water vapour on synoptical situations e.g. low pressure systems and on more climatological phenomena e.g. El Nino or the NAO should be investigated.

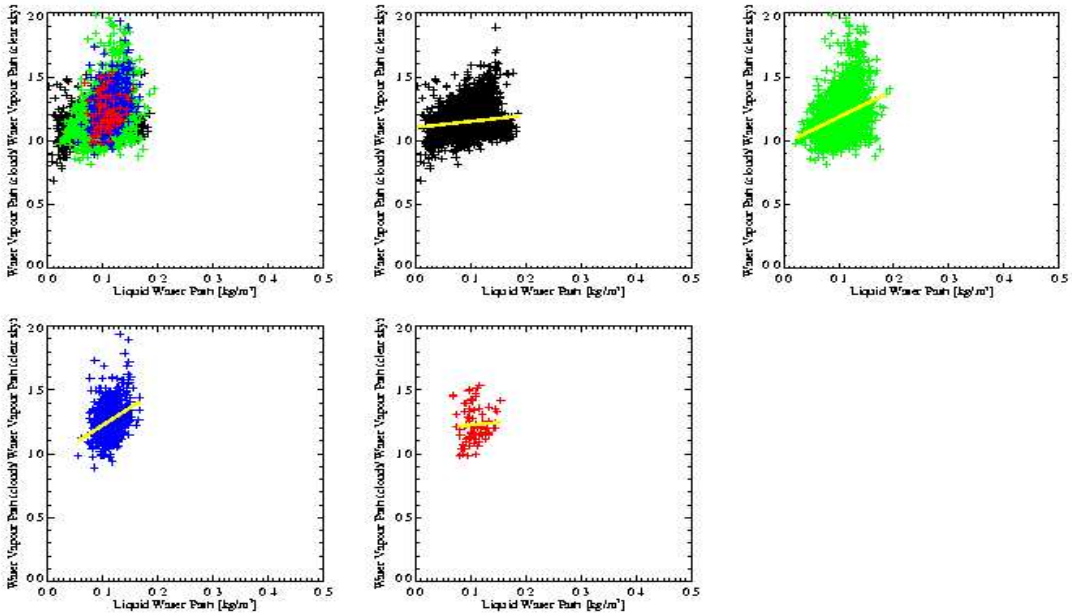

Figure 4.5: *Excess Water Vapour (WVP (cloudy)/WVP (clear)) vs LWP, monthly mean on a 2.5°× 2.5° grid for the North Atlantic. Black: 0-30° North, green: 30-50° North, blue: 50-60° North and red: 60-90° North. The yellow line represents the regression. (February to December 2001).*

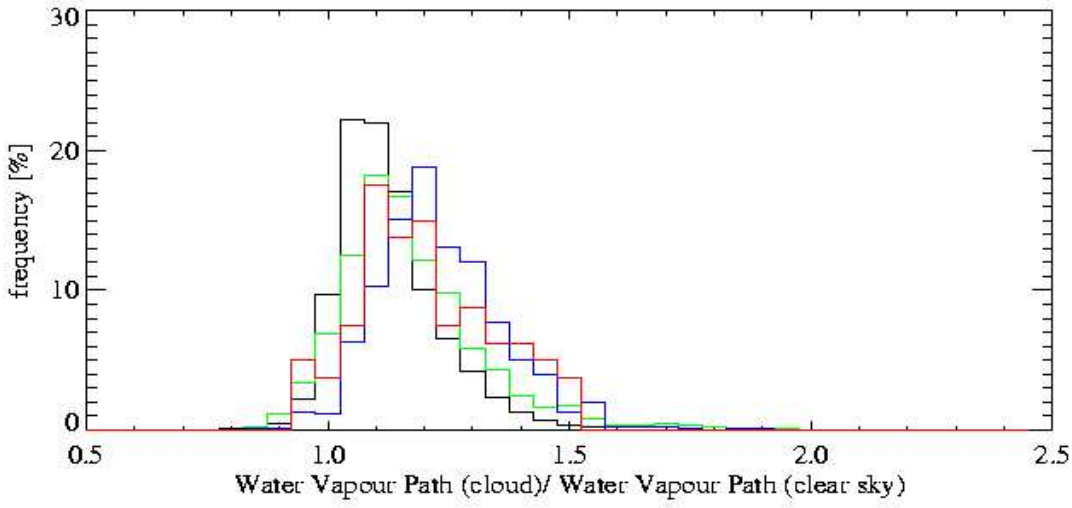

Figure 4.6: *Frequency distribution of the excess Water Vapour (WVP(cloudy)/WVP(clear)), monthly mean on a 2.5°× 2.5° grid for the North Atlantic. Black: 0-30° North, green: 30-50° North, blue: 50-60° North and red: 60-90° North. (February to December 2001).*

Chapter 5

Conclusions

The present study performed a first estimate of the water vapour excess in cloudy areas compared to the more easily retrievable clear sky areas. Starting from the limited number of AVHRR cases the cloud cover inside an AMSU field of view plays no significant role when deriving the relation between clear and cloudy water vapour path. With more advanced AVHRR cloud detection and cloud classification schemes which include the retrieval during night time the influence on cloud cover and cloud type can be further investigated. In this context we recommend to take advantage of the cloud retrieval scheme developed at SMHI and the cloud physical property retrieval as built at the KNMI in the framework of the CM–SAF.

It is expected that the water vapour excess in cloudy areas depends on cloud type. On the global scale the water vapour path frequency distributions show a bimodal structure for all oceans. Seperated in the northern and southern part the bimodal structure is weak because of the movement of the inner tropical convergence zone. Thus, dominant situations with large and low atmospheric humidity exist and should be treated separately when accounting for excess water vapour. Again, with the aid of advanced cloud classification and cloud retrieval schemes, the relation between cloud type and water vapour excess can be considerably improved.

The correlation between the water vapour path and the liquid water path is less pronounced for the whole North Atlantic ocean. A detailed analysis shows that the correlation depends on the climatological regime. For the high cumulus towers and shallow cumulus in the tropics and the subtropical regions, the correlation is lower than for more stratiform cloudy areas in the mid-latitudes and the polar regions. On climatological scales the water vapour path in clear skies is 83% of the water vapour path in cloudy atmospheres. Which almost perfectly coincides with experimental results from the EU-Project CLIWA–NET over land areas for August and September 2000. Thus, it appears reasonable to obtain cloudy sky water vapour structures from nearby clear sky sounding and additional cloud informations. The present study is based on NOAA–16 overpasses from 2001 only. For a more general analysis more and other satellite informations should be included. The excess water vapour retrieved from AQUA measurements show values of the same magnitude on global scale as our study. The median of the excess water vapour distribution is slightly higher, with 1.5, then the one derived here (private communications with Chris O'Dell, University Wisconsin, Madison).

Furthermore, it is recommended to make use of the NCEP/NCAR reanalysis data to correlate the excess water vapour retrieved from satellite and ground data and synoptical (e.g. low pressure systems) and climatological (e.g. NAO, ENSO) situations. A number of studies performed at the IFM-GEOMAR have demonstrated that the advection of water vapour from the Atlantic Ocean towards Europe is basically driven by the NAO pattern (Ruprecht et al. (2002) and Ruprecht und Kahl (2003)). The present work did account for NCEP/NCAR SST and wind informations on pixel scale. However, identification of the underlying large to medium scale atmospheric pattern was beyond the scope of this 3 month study.

In the above described context of cloud classification and retrieval of cloud physical properties we suggest to improve these schemes to better account for ice clouds (or icy cloud tops) and 3d radiative transfer effects, because errors in cloud retrieval due to miss-interpretation of cloud type induce large errors in the retrieval of cloud water vs. water vapor relationships.

Bibliography

Crewell, S. und U. Löhnert. Accuracy of cloud liquid water path from ground-based microwave radiometry - 2. Sensor accuracy and synergy. *Radio Science*, 38(3) (2003).

Crewell, S. et al. Cloud observations and modeling within the European BALTEX Cloud Liquid Water Network. *Boreal Environment Research*, 7: 235–245 (2002).

Cruz Pol, S. et al. Improved 20 - to 32 - GHz atmospheric absorption model. *Radio Science*, 33: 1319 – 1333 (1998).

Grody, N. et al. Determination of precipitable water and cloud liquid water over oceans from the NOAA-15 advanced microwave sounding unit. *Journal of Geophysical Research*, 106(D3): 2943–2953 (2001).

Hargens, U. Remote Sensing of Cloud Liquid Water during ICE'89. IEEE Trans. Microwave Theory and Tech. Soc. (1992).

IPCC Working Group I. *Climate Change 2001: The Scientific Basis. Contributions of Working Group I to the third Assessment Report of the intergovernmental Panel on Climate Change*. Cambridge University Press, Cambridge, United Kingdom and New York, NY, USA (2001).

Kalnay, E. und Coauthors. The NCEP/NCAR 40-years reanalysis project. *Bulletin American Meteorological Society*, 77: 437 – 471 (1996).

König-Langlo, G. und B. Marx. *The Meteorological Information System at the Alfred Wegener Institute*. Kluwer Academic Publisher (1997). Printed in USA Norwell.

Liebe, H. MPM – An atmospheric milimeter-wave propagation model. *Int. J. Infrared Milimeter Waves*, 10: 631 – 650 (1989).

Liebe, H. et al. Propagation modelling of moist air and suspended water/ice particles at Frequencies below 100 GHz. *Paper presented at AGARD 52nd Special Meeting of the Panel on Electromagnetic Wave Propagation, Adv. Group for Aerosp. Res. and Dev., Palma de Mallorca, Spain, 17 - 21 May, 1993* (1993).

NOAA-KLM Users Guide, . *NOAA-KLM Users Guide, http://www2.ncdc.noaa.gov/docs/klm/index.htm* (1998).

Rosenkranz, P. Water Vapour Microwave Continuum Absorption: A Comparison of Measurements and Models. *Radio Science*, 33: 919 – 928 (1998). (Correction, Radio Science, 34, 1025, 1999).

Ruprecht, E. und T. Kahl. Investigation of the atmospheric water budget of the BALTEX area using NCEP/NCAR reanalysis data. *Tellus*, 55a: 426–437 (2003).

Ruprecht, E. et al. On the relation of the NAO and water vapour transport towards Europe. *Meteorologische Zeitschrift*, 11: 701–702 (2002).

Simmer, C. *Satellitenfernerkundung hydrologischer Parameter der Atmosphäre mit Mikrowellen.* Verlag Dr. Kovaŏc, Hamburg (1994).

Ulaby, F. et al. *Microwave Remote Sensing, Active and Passive.* Artech House INC., Norwood,MA (1981).

von Bremen, L. et al. Errors in Liquid Water Path Retrieval arising from Cloud Inhomogeneities: The Beamfilling Effect. *Meteorologische Zeitschrift*, 11(1): 13–19 (2002).

Wahl, S. et al. Precipitable Water in Cloudy Areas. *VS-Plan 7.7*, Seite 26 (2003).

Appendix A

List of Acronyms and Symbols

AMSU	Advanced Microwave Sounding Unit
AVHRR	Advanced Very High Resolution Radiometer
CLIWA-NET	Cloud Liquid Water Network
CM–SAF	Climate Monitoring Satellite Application Facility
ENSO	El Nino Southern Oscillation
FOV	Field of View
KNMI	Koninklijk Nedelands Meteorologisch Instituut
LWP	Liquid Water Path
NAO	North Atlantic Oscillation
NCAR	National Center for Atmospheric Research
NCEP	National Center for Environmental Prediction
NN	Neural Network
NOAA	National Oceanic and Atmospheric Asotiation
SSM/I	Special Sensor Microwave Imager
T_B	Brightness temperature
T_S	Surface Temperature
TPW	Total Precipitable Water
WVP	Water Vapour Path

Appendix B

Cloud Cover

For noon overpasses the cloud cover of a grid box is retrieved. For this purpose the AVHRR channels are used as described in Chapter 2.2. The spatial mean LWP and WVP are correlated depending on the cloud cover of the grid cell. In figure B1 the relation for a $4.0° \times 4.0°$ grid is shown. There are no dependencies found of the cloud cover to the correlation of the mean LWP to the WVP. Similar results are shown in figure B2 for a $1.0° \times 1.0°$ grid.

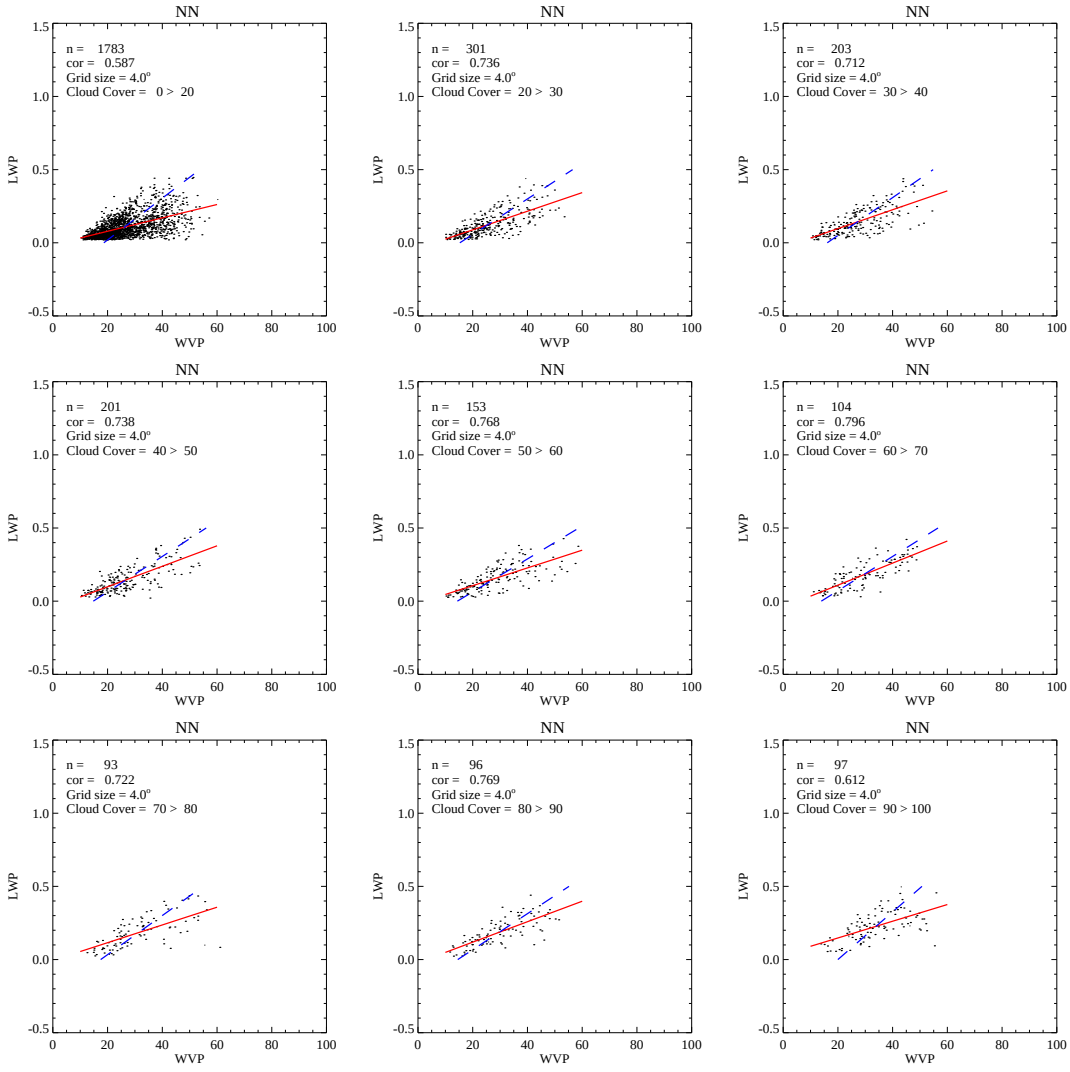

Figure B.1: *Influence of cloud cover on the relation LWP to WVP. LWP is given in kg/m^2 and the WVP in kg/m^2. The retrieved values are sampled on a 4.0°× 4.0° grid.*

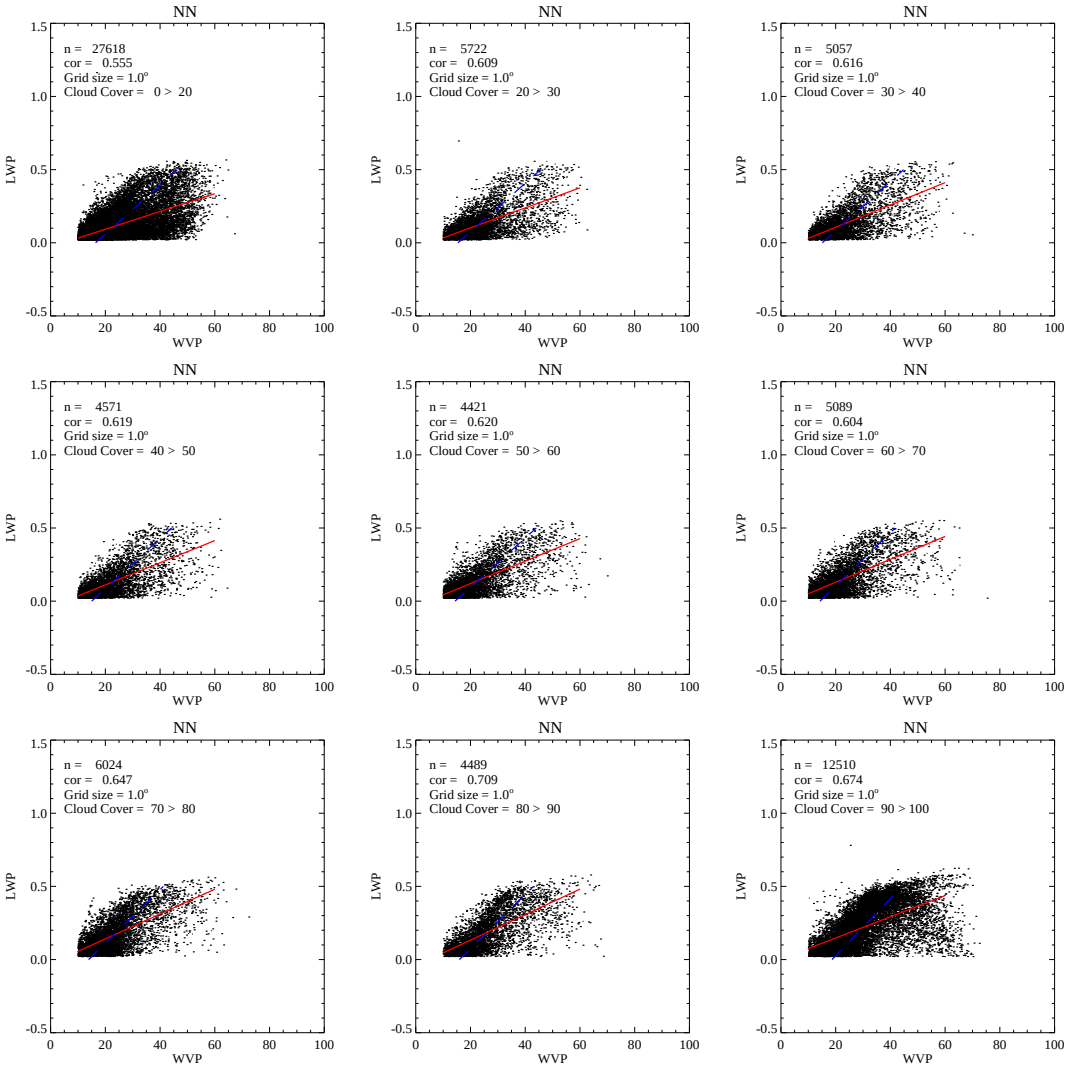

Figure B.2: *Influence of cloud cover on the relation LWP to WVP. LWP is given in kg/m^2 and the WVP in kg/m^2. The retrieved values are sampled on a 1.0°× 1.0° grid.*

Appendix C

Frequency distributions

The distribution of the WVP and LWP on a 1.0° grid is shown in figure C1. For the WVP a bimodal structure is found for the global ocean. A seperate regard of the ocean basins and by the northern and southern part show, that the peak at high water vapour path is not strongly present. A cause can be found in the movement of the inner tropical convergence zone over the year.

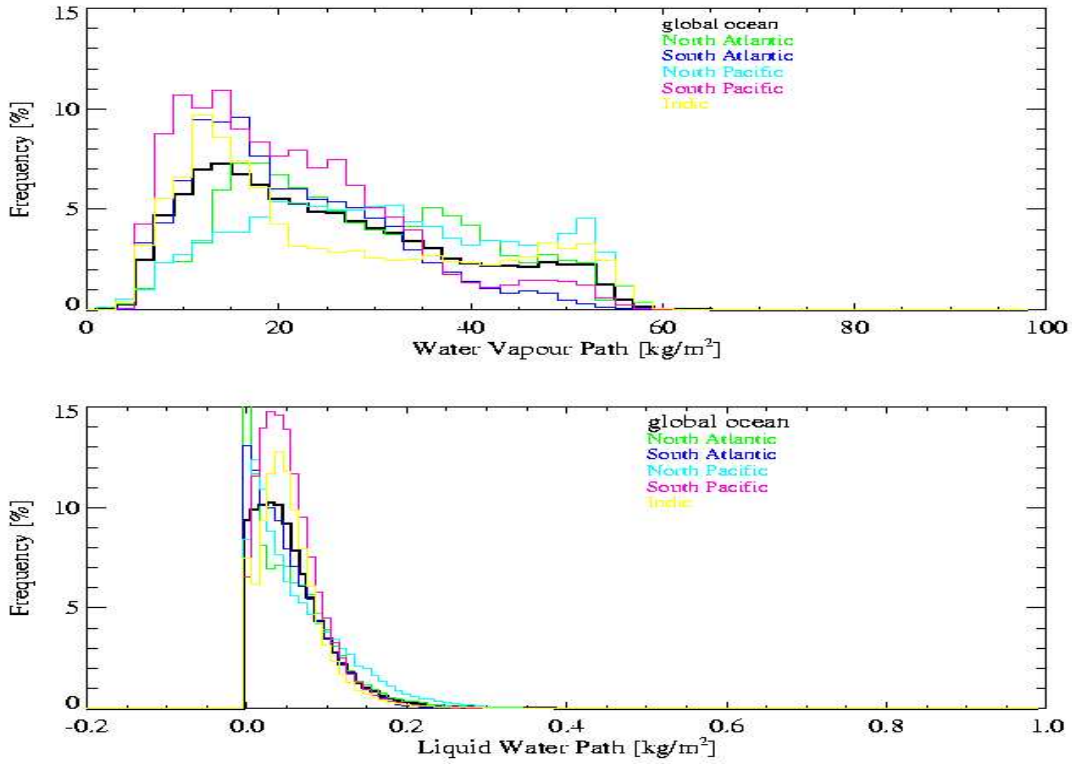

Figure C.1: WVP(upper) and LWP(lower) frequency distributions relative to the covered amount of pixels on a 1.0° grid. Monthly means are shown. (February to December 2001).

Appendix D

Water Vapour Enhancement

The interrelation of LWP and WVP is shown for the whole periode (February to December 2001) for the North Atlantic ocean and seperated by the latitude, see figure D1. The fragmentation by latitude corresponds to a coarse separation by the dominant cloud types in the regional interval and reflects the latitudinal distribution of WVP. The tropics (black) represent the high cumulus towers as a dominant feature. Shallow cumulus in the sub-tropics (green) lead to a low correlation because of the small amount of LWP sampled over the grid. The correlation increases in the mid- and high–latitudes, where the stratiform clouds are the dominant feature. In figure D2 the water vapour enhancement, represented by the ratio of cloudy WVP by clear WVP, is shown versus the clear sky WVP. The ratio varies from 1.0 to 1.5 with a median at 1.2, figure D4, which means that the WVP in clear skys is 83% of the cloudy WVP. The ratio is depending on the LWP as shown in D3.
This factor varies slightly through the seasons (March to May (figures D5–D8), June to August (figures D9–D12) and September to November (figures D13–D16) 2001).

The METEOSAT disk covers the southern Atlantic as well. In figures D17–D32 the analysis for the excess water vapour is shown. The retrieved factors for the North Atlantic coinsides with the one retrieved for the South Atlantic.

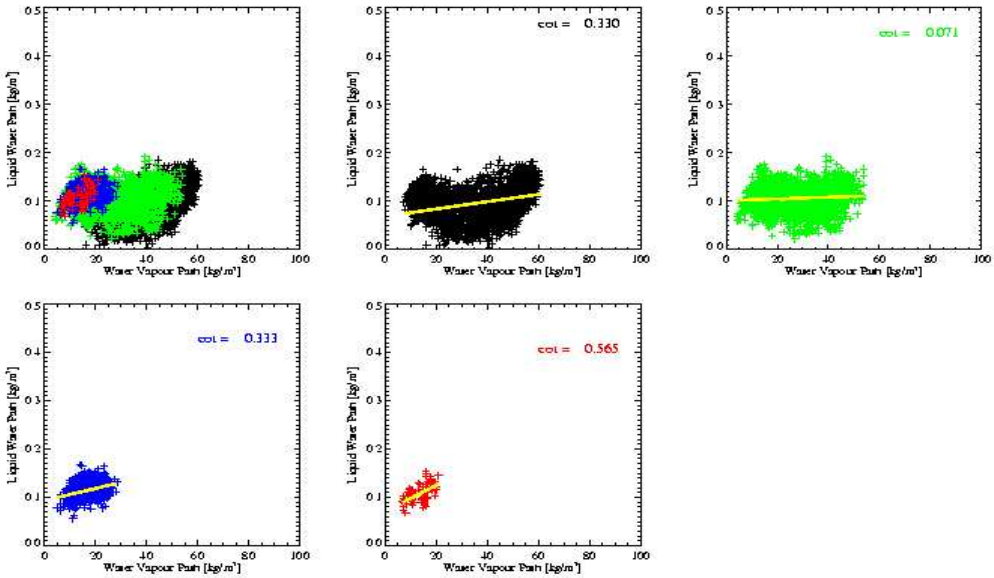

Figure D.1: *Water Vapour Path vs LWP, monthly mean on a 2.5°× 2.5° grid for the North Atlantic. Black: 0-30° North, green: 30-50° North, blue: 50-60° North and red: 60-90° North. In yellow the regression is presented. (February to December 2001).*

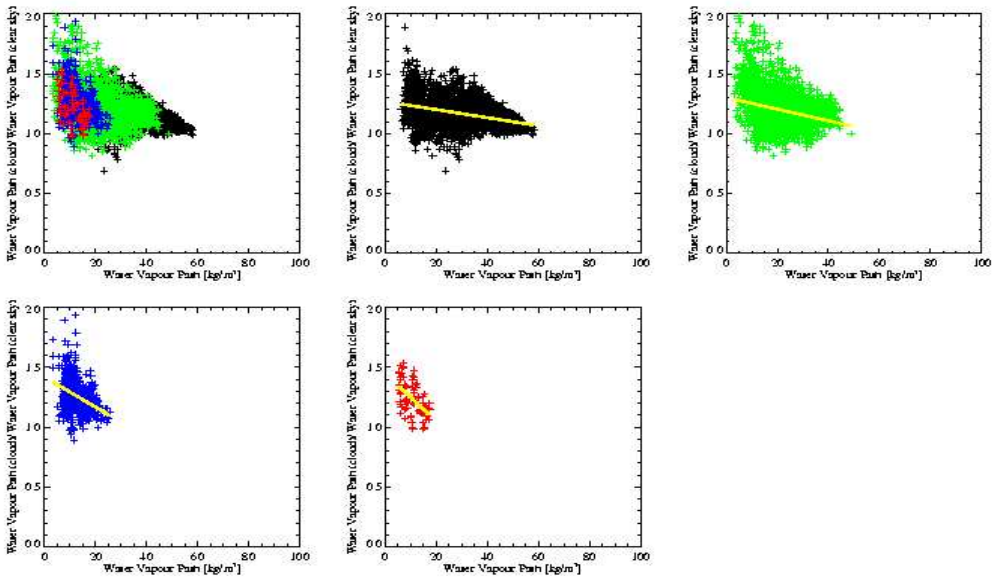

Figure D.2: *Excess Water Vapour (WVP(cloudy)/WVP(clear)) vs WVP for clear cases, monthly mean on a 2.5°× 2.5° grid for the North Atlantic. Black: 0-30° North, green: 30-50° North, blue: 50-60° North and red: 60-90° North. In yellow the regression is presented. (February to December 2001).*

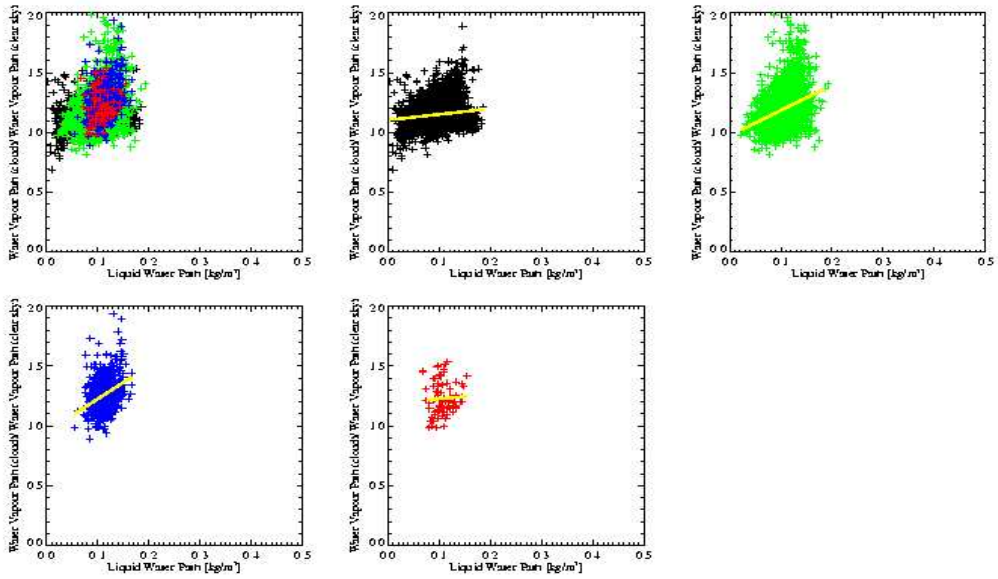

Figure D.3: *Excess Water Vapour (WVP(cloudy)/WVP(clear)) vs LWP, monthly mean on a 2.5°× 2.5° grid for the North Atlantic. Black: 0-30° North, green: 30-50° North, blue: 50-60° North and red: 60-90° North. In yellow the regression is presented. (February to December 2001).*

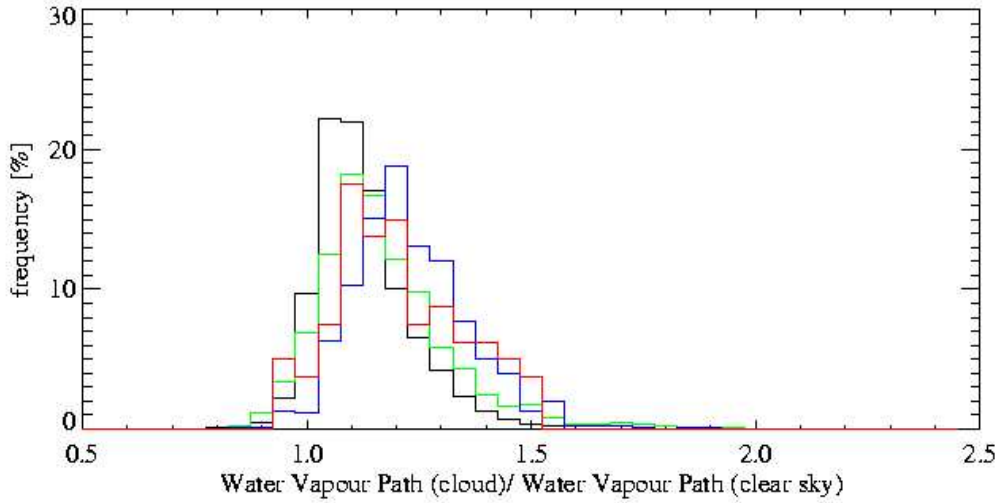

Figure D.4: *Frequency distribution of the excess Water Vapour (WVP(cloudy)/WVP(clear)), monthly mean on a 2.5°× 2.5° grid for the North Atlantic. Black: 0-30° North, green: 30-50° North, blue: 50-60° North and red: 60-90° North. (February to December 2001).*

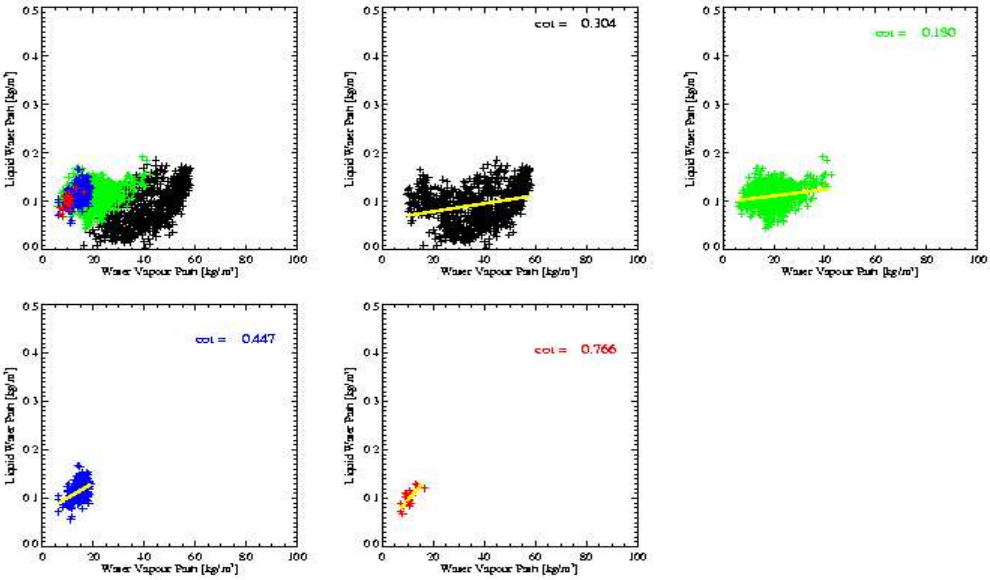

Figure D.5: *Water Vapour Path vs LWP, monthly mean on a 2.5°× 2.5° grid for the North Atlantic. Black: 0-30° North, green: 30-50° North, blue: 50-60° North and red: 60-90° North. In yellow the regression is presented. (March to May 2001).*

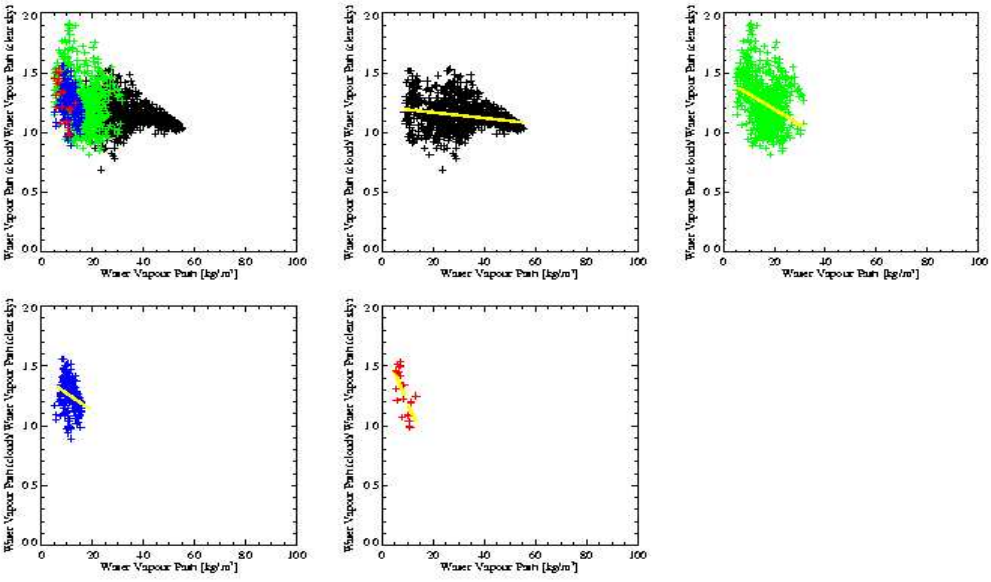

Figure D.6: *Excess Water Vapour (WVP(cloudy)/WVP(clear)) vs WVP for clear cases, monthly mean on a 2.5°× 2.5° grid for the North Atlantic. Black: 0-30° North, green: 30-50° North, blue: 50-60° North and red: 60-90° North. In yellow the regression is presented. (March to May 2001).*

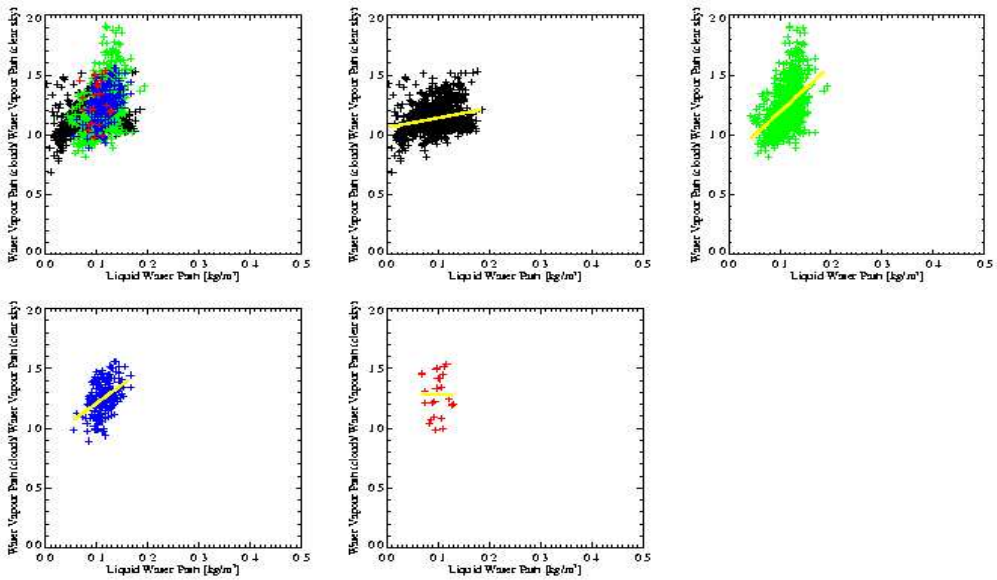

Figure D.7: *Excess Water Vapour (WVP(cloudy)/WVP(clear)) vs LWP, monthly mean on a 2.5°× 2.5° grid for the North Atlantic. Black: 0-30° North, green: 30-50° North, blue: 50-60° North and red: 60-90° North. In yellow the regression is presented. (March to May 2001).*

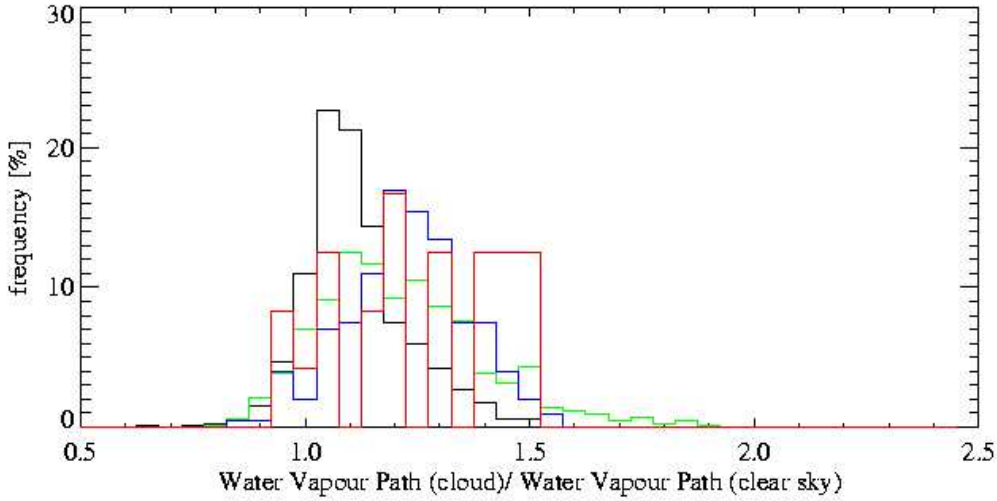

Figure D.8: *Frequency distributoin of the excess Water Vapour (WVP(cloudy)/WVP(clear)), monthly mean on a 2.5°× 2.5° grid for the North Atlantic. Black: 0-30° North, green: 30-50° North, blue: 50-60° North and red: 60-90° North. (March to May 2001).*

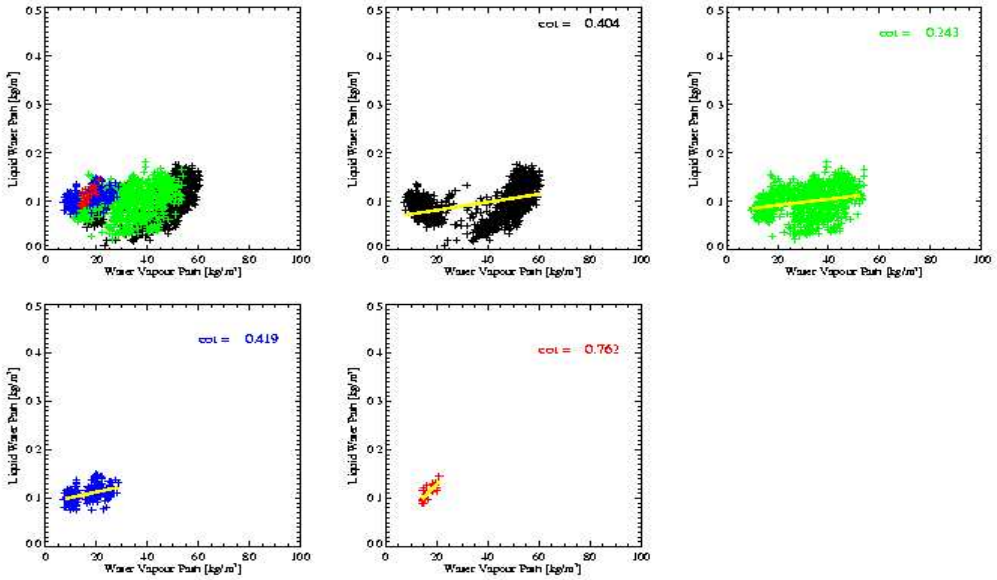

Figure D.9: *Water Vapour Path vs LWP, monthly mean on a 2.5°× 2.5° grid for the North Atlantic. Black: 0-30° North, green: 30-50° North, blue: 50-60° North and red: 60-90° North. In yellow the regression is presented. (June to August 2001).*

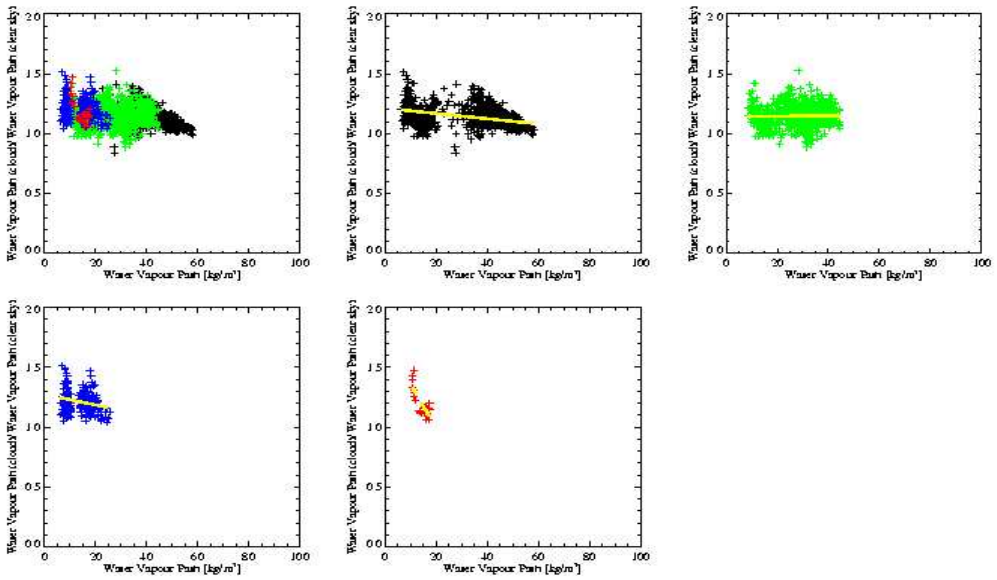

Figure D.10: *Excess Water Vapour (WVP(cloudy)/WVP(clear)) vs WVP for clear cases, monthly mean on a 2.5°× 2.5° grid for the North Atlantic. Black: 0-30° North, green: 30-50° North, blue: 50-60° North and red: 60-90° North. In yellow the regression is presented. (June to August 2001).*

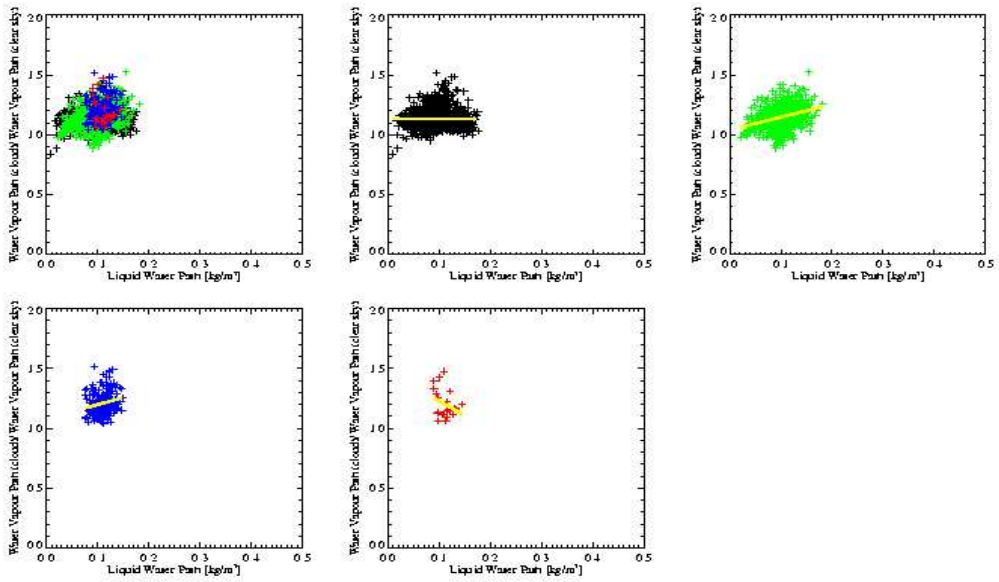

Figure D.11: *Excess Water Vapour (WVP(cloudy)/WVP(clear)) vs LWP, monthly mean on a 2.5°× 2.5° grid for the North Atlantic. Black: 0-30° North, green: 30-50° North, blue: 50-60° North and red: 60-90° North. In yellow the regression is presented. (June to August 2001).*

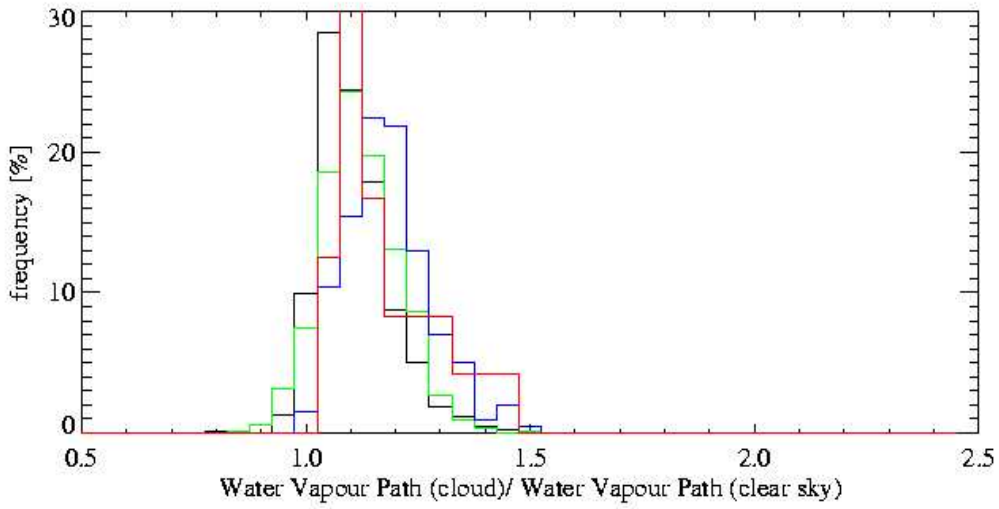

Figure D.12: *Frequency distribution of the excess Water Vapour (WVP(cloudy)/WVP(clear)), monthly mean on a 2.5°× 2.5° grid for the North Atlantic. Black: 0-30° North, green: 30-50° North, blue: 50-60° North and red: 60-90° North. (June to August 2001).*

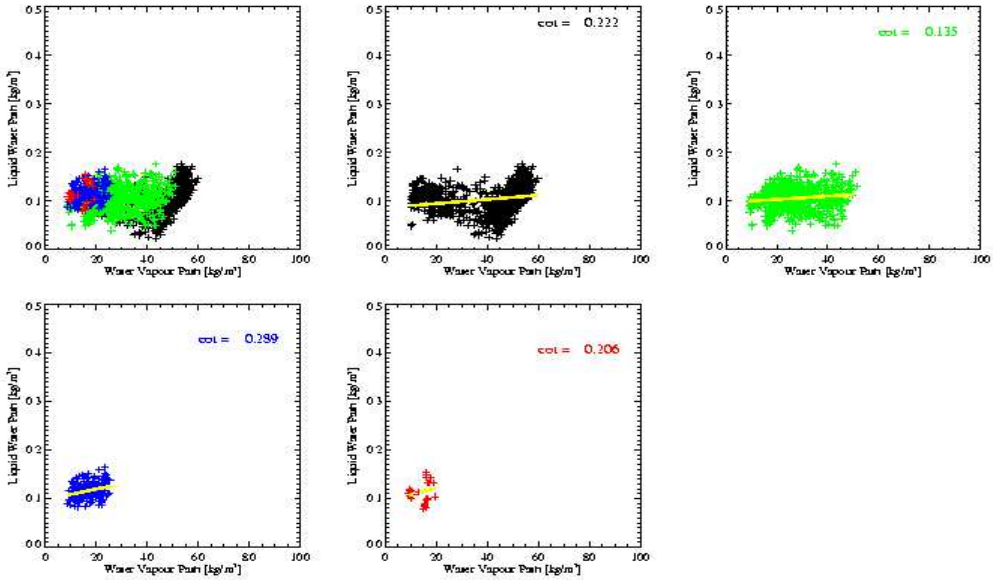

Figure D.13: *Water Vapour Path vs LWP, monthly mean on a 2.5°× 2.5° grid for the North Atlantic. Black: 0-30° North, green: 30-50° North, blue: 50-60° North and red: 60-90° North. In yellow the regression is presented. (September to November 2001).*

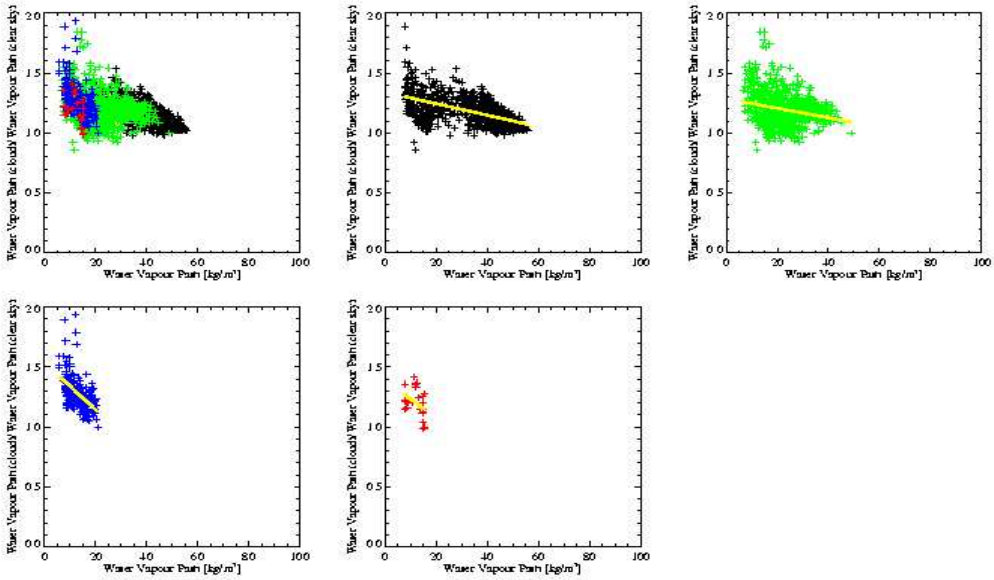

Figure D.14: *Excess Water Vapour (WVP(cloudy)/WVP(clear)) vs WVP for clear cases, monthly mean on a 2.5°× 2.5° grid for the North Atlantic. Black: 0-30° North, green: 30-50° North, blue: 50-60° North and red: 60-90° North. In yellow the regression is presented. (September to November 2001).*

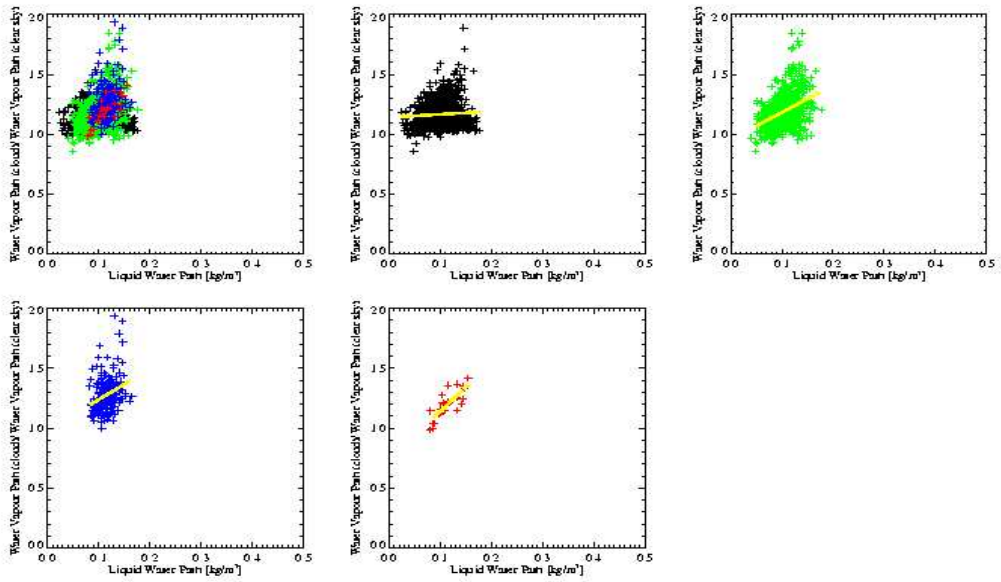

Figure D.15: *Excess Water Vapour (WVP(cloudy)/WVP(clear)) vs LWP, monthly mean on a 2.5°× 2.5° grid for the North Atlantic. Black: 0-30° North, green: 30-50° North, blue: 50-60° North and red: 60-90° North. In yellow the regression is presented. (September to November 2001).*

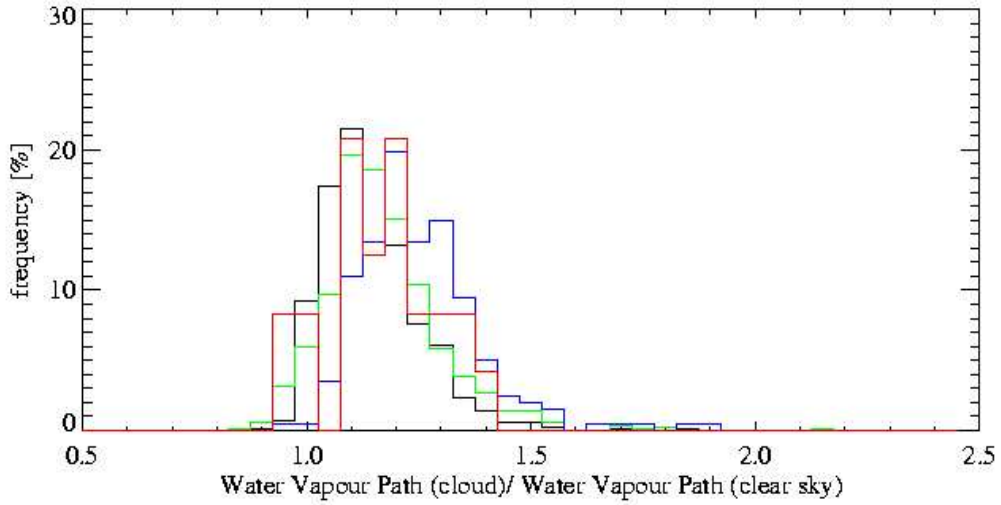

Figure D.16: *Frequency distribution of the excess Water Vapour (WVP(cloudy)/WVP(clear)), monthly mean on a 2.5°× 2.5° grid for the North Atlantic. Black: 0-30° North, green: 30-50° North, blue: 50-60° North and red: 60-90° North. (September to November 2001).*

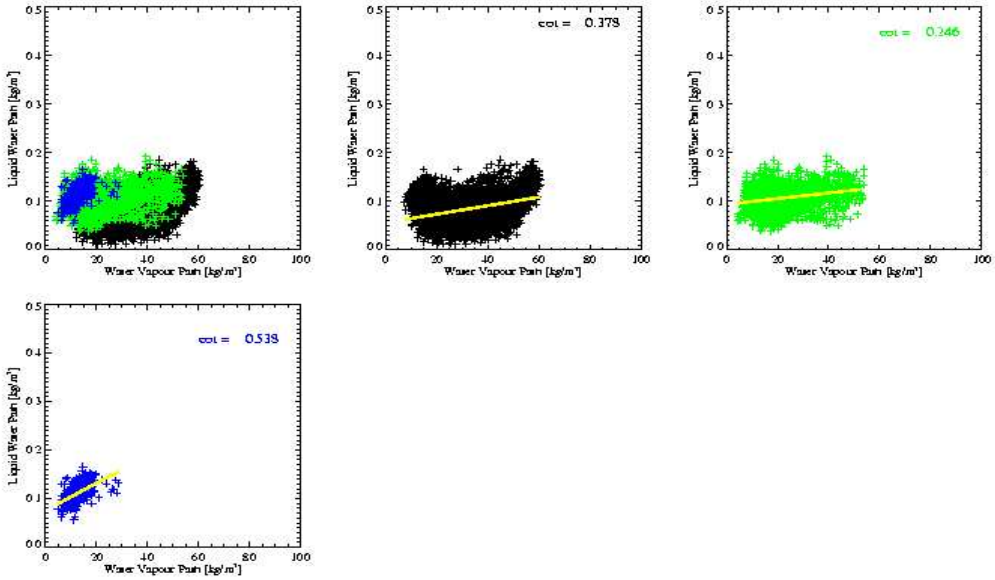

Figure D.17: *Water Vapour Path vs LWP, monthly mean on a 2.5°× 2.5° grid for the South Atlantic. Black: 0-30° South, green: 30-50° South, blue: 50-60° South. The yellow line represents the regression. (February to December 2001).*

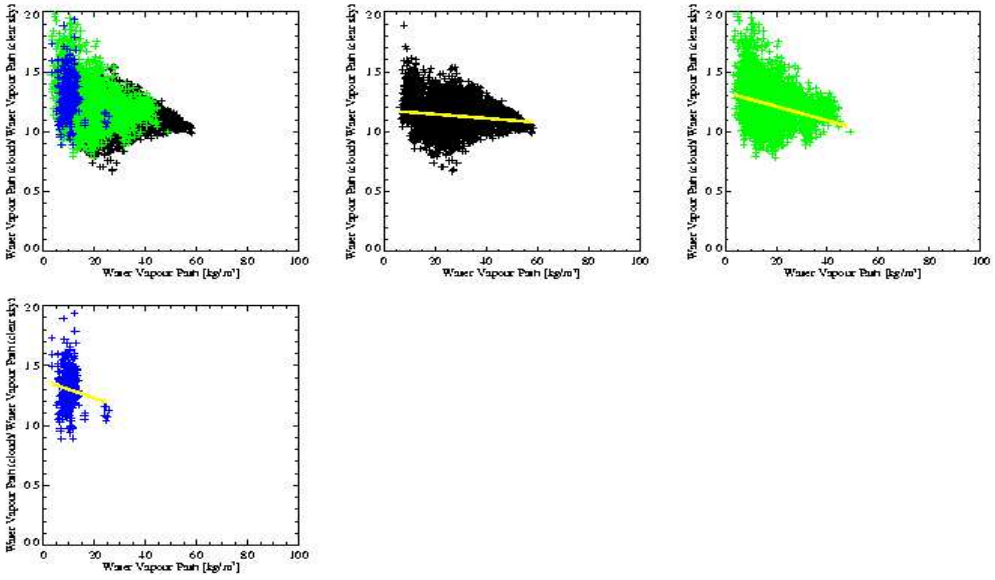

Figure D.18: *Excess Water Vapour (WVP(cloudy)/WVP(clear)) vs WVP for clear cases, monthly mean on a 2.5°× 2.5° grid for the South Atlantic. Black: 0-30° South, green: 30-50° South, blue: 50-60° South. The yellow line represents the regression. (February to December 2001).*

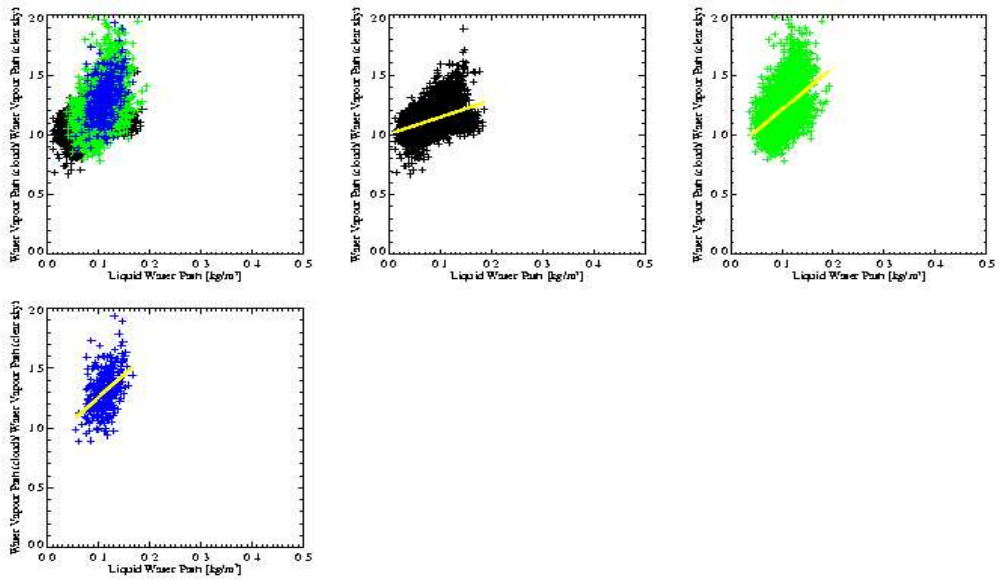

Figure D.19: *Excess Water Vapour (WVP(cloudy)/WVP(clear)) vs LWP, monthly mean on a 2.5°× 2.5° grid for the South Atlantic. Black: 0-30° South, green: 30-50° South, blue: 50-60° South. The yellow line represents the regression. (February to December 2001).*

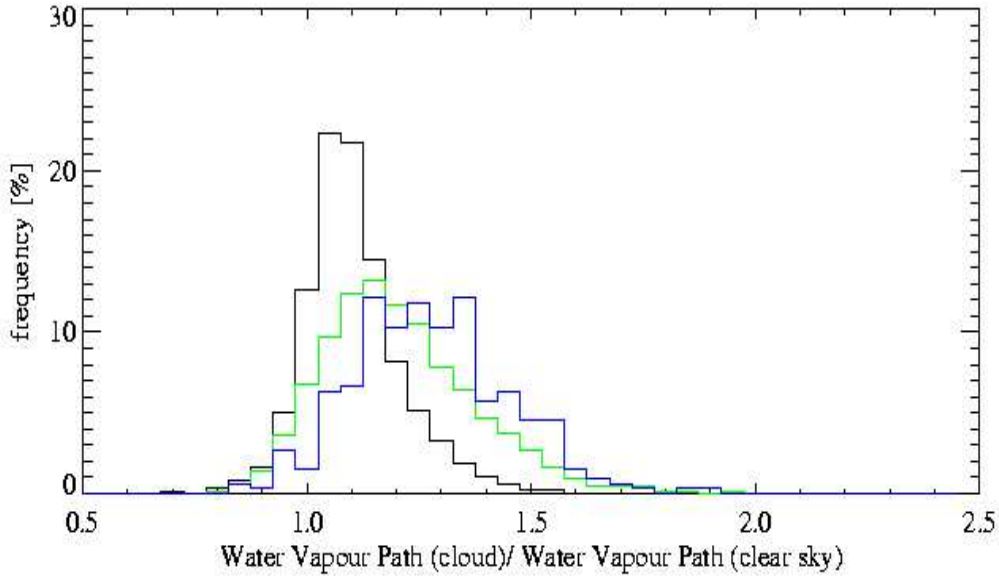

Figure D.20: *Frequency distribution of the excess Water Vapour (WVP(cloudy)/WVP(clear)) vs LWP, monthly mean on a 2.5°× 2.5° grid for the South Atlantic. Black: 0-30° South, green: 30-50° South, blue: 50-60° South. (February to December 2001).*

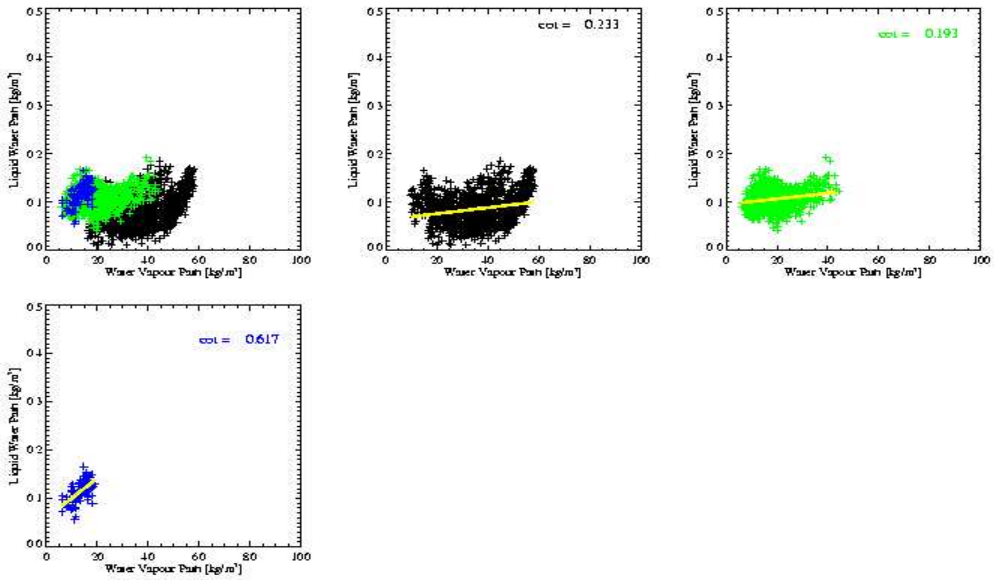

Figure D.21: *Water Vapour Path vs LWP, monthly mean on a 2.5°× 2.5° grid for the South Atlantic. Black: 0-30° South, green: 30-50° South, blue: 50-60° South. The yellow line represents the regression. (March to May 2001).*

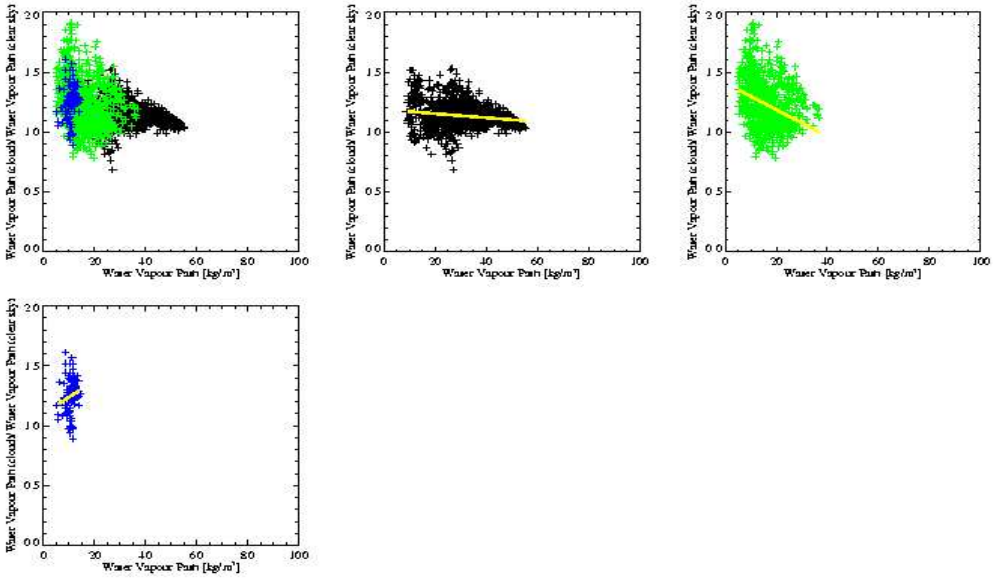

Figure D.22: *Excess Water Vapour (WVP(cloudy)/WVP(clear)) vs WVP for clear cases, monthly mean on a 2.5°× 2.5° grid for the South Atlantic. Black: 0-30° South, green: 30-50° South, blue: 50-60° South. The yellow line represents the regression. (March to May 2001).*

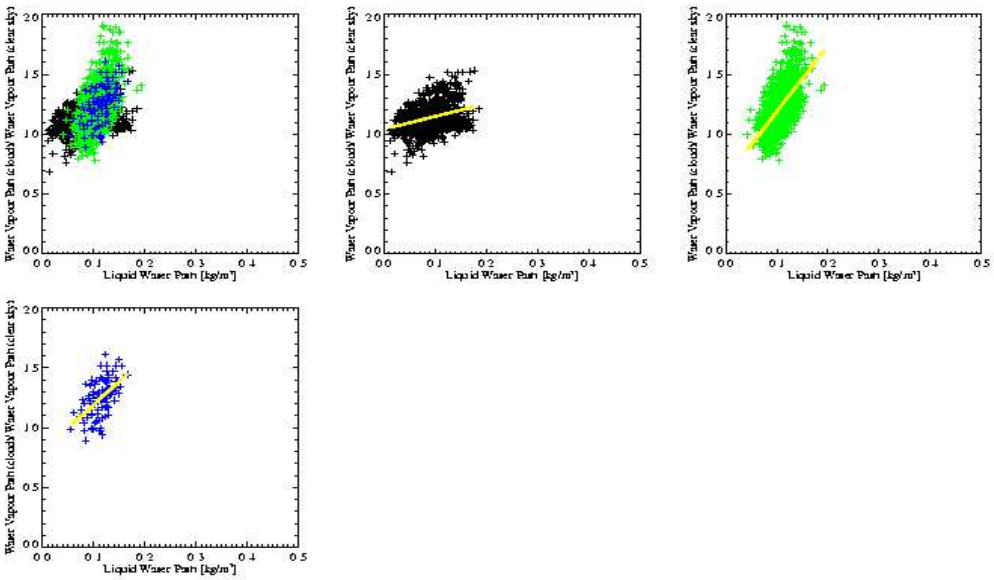

Figure D.23: *Excess Water Vapour (WVP(cloudy)/WVP(clear)) vs LWP, monthly mean on a 2.5°× 2.5° grid for the South Atlantic. Black: 0-30° South, green: 30-50° South, blue: 50-60° South. The yellow line represents the regression. (March to May 2001).*

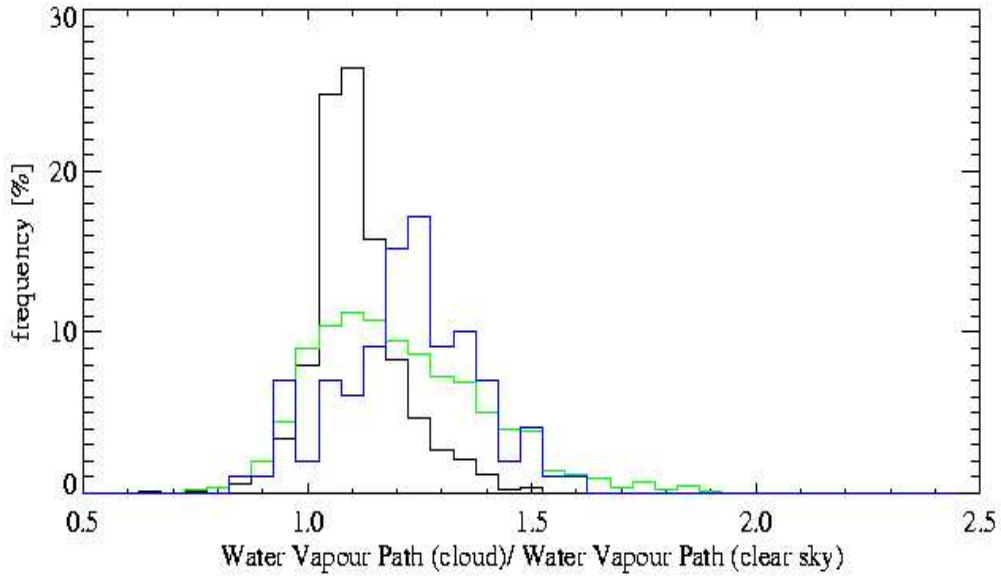

Figure D.24: *Frequency distribution of the excess Water Vapour (WVP(cloudy)/WVP(clear)) vs LWP, monthly mean on a 2.5°× 2.5° grid for the South Atlantic. Black: 0-30° South, green: 30-50° South, blue: 50-60° South. (March to May 2001).*

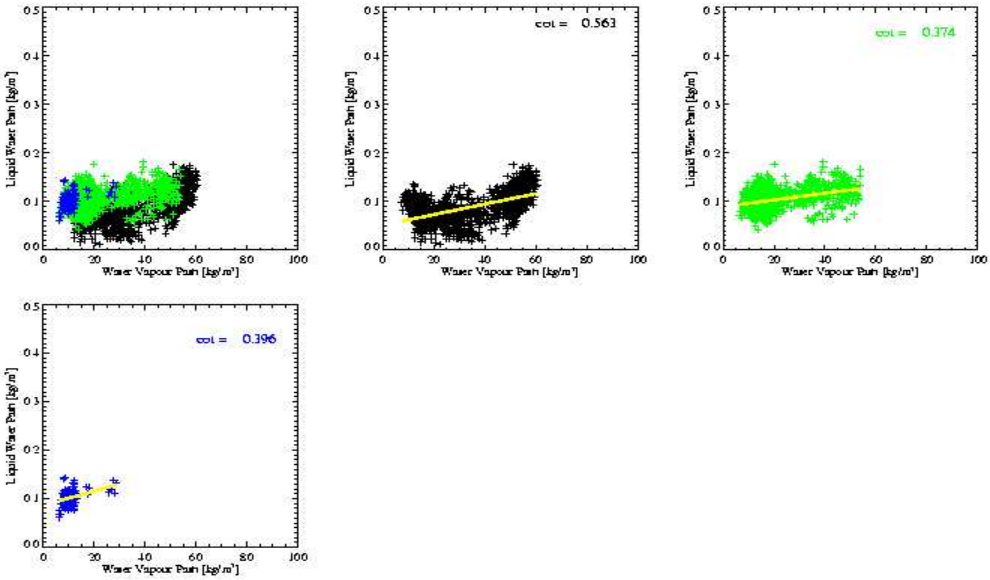

Figure D.25: *Water Vapour Path vs LWP, monthly mean on a 2.5°× 2.5° grid for the South Atlantic. Black: 0-30° South, green: 30-50° South, blue: 50-60° South. The yellow line represents the regression. (June to August 2001).*

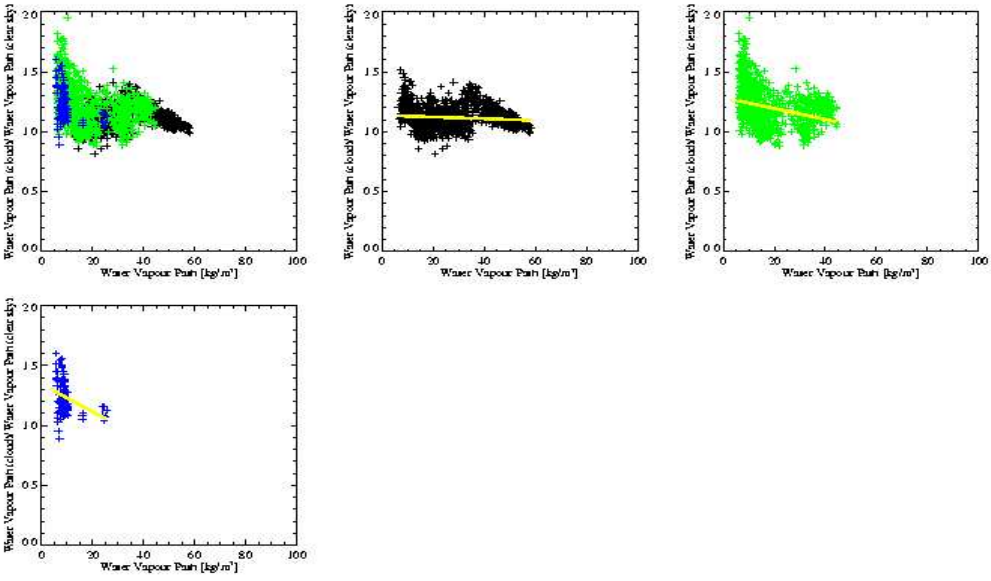

Figure D.26: *Excess Water Vapour (WVP(cloudy)/WVP(clear)) vs WVP for clear cases, monthly mean on a 2.5°× 2.5° grid for the South Atlantic. Black: 0-30° South, green: 30-50° South, blue: 50-60° South. The yellow line represents the regression. (June to August 2001).*

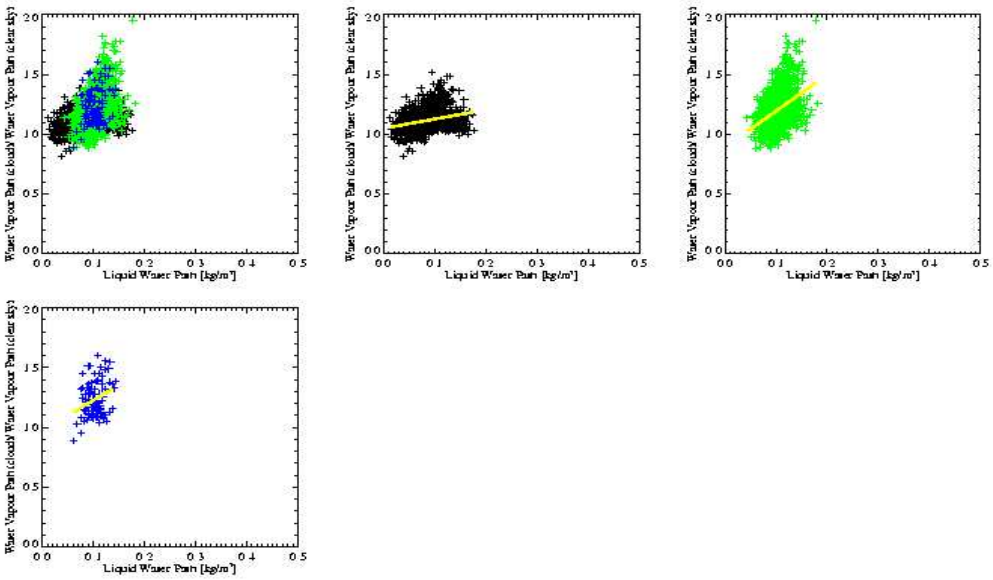

Figure D.27: *Excess Water Vapour (WVP(cloudy)/WVP(clear)) vs LWP, monthly mean on a 2.5°× 2.5° grid for the South Atlantic. Black: 0-30° South, green: 30-50° South, blue: 50-60° South. The yellow line represents the regression. (June to August 2001).*

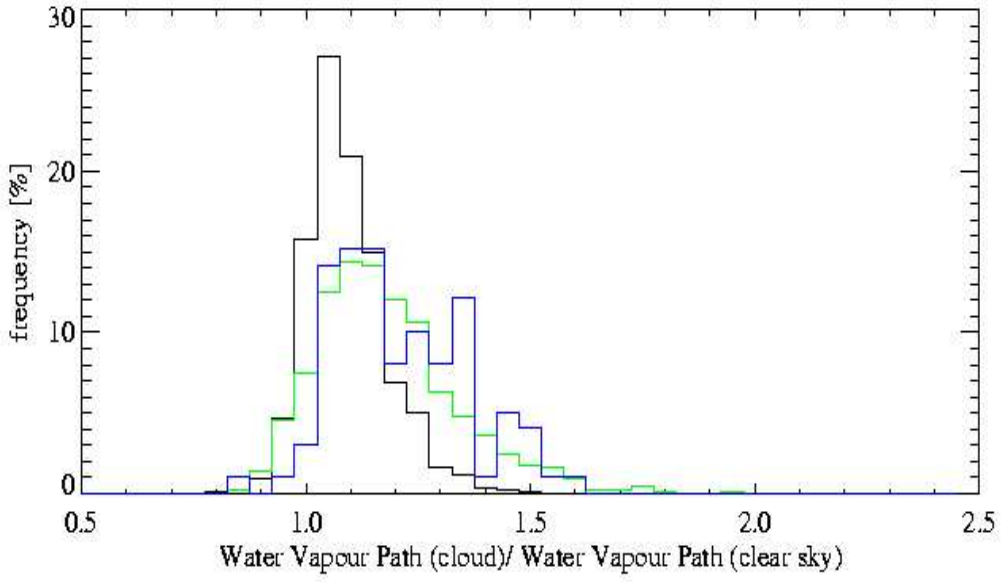

Figure D.28: *Frequency distribution of the excess Water Vapour (WVP(cloudy)/WVP(clear)) vs LWP, monthly mean on a 2.5°× 2.5° grid for the South Atlantic. Black: 0-30° South, green: 30-50° South, blue: 50-60° South. (June to August 2001).*

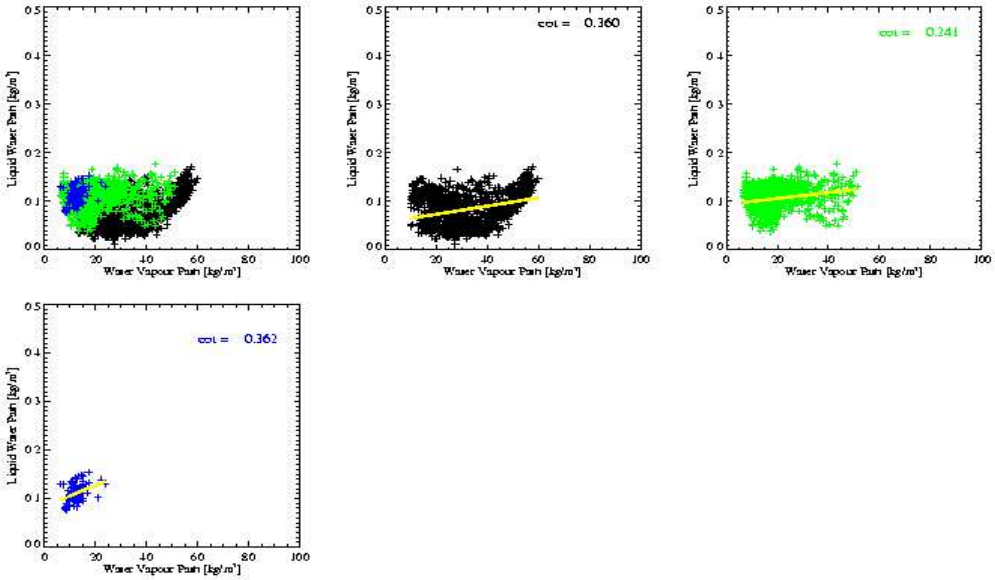

Figure D.29: *Water Vapour Path vs LWP, monthly mean on a 2.5°× 2.5° grid for the South Atlantic. Black: 0-30° South, green: 30-50° South, blue: 50-60° South. The yellow line represents the regression. (September to November 2001).*

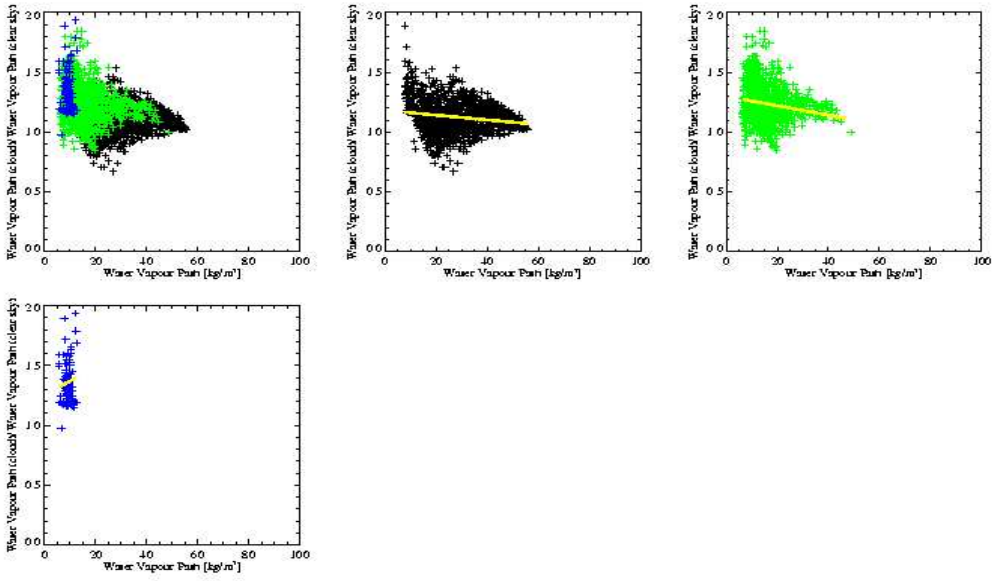

Figure D.30: *Excess Water Vapour (WVP(cloudy)/WVP(clear)) vs WVP for clear cases, monthly mean on a 2.5°× 2.5° grid for the South Atlantic. Black: 0-30° South, green: 30-50° South, blue: 50-60° South. The yellow line represents the regression. (September to December 2001).*

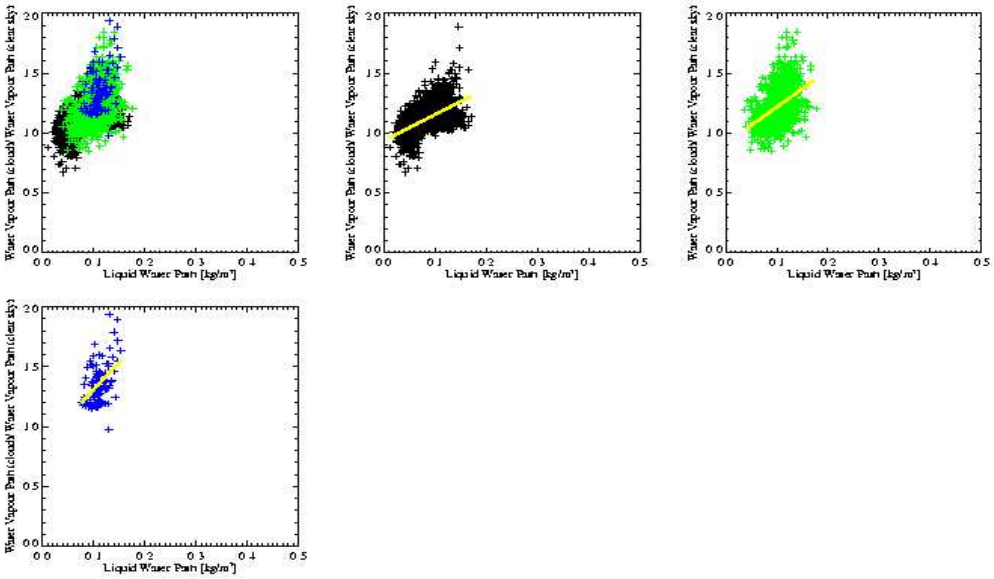

Figure D.31: *Excess Water Vapour (WVP(cloudy)/WVP(clear)) vs LWP, monthly mean on a 2.5°× 2.5° grid for the South Atlantic. Black: 0-30° South, green: 30-50° South, blue: 50-60° South. The yellow line represents the regression. (September to November 2001).*

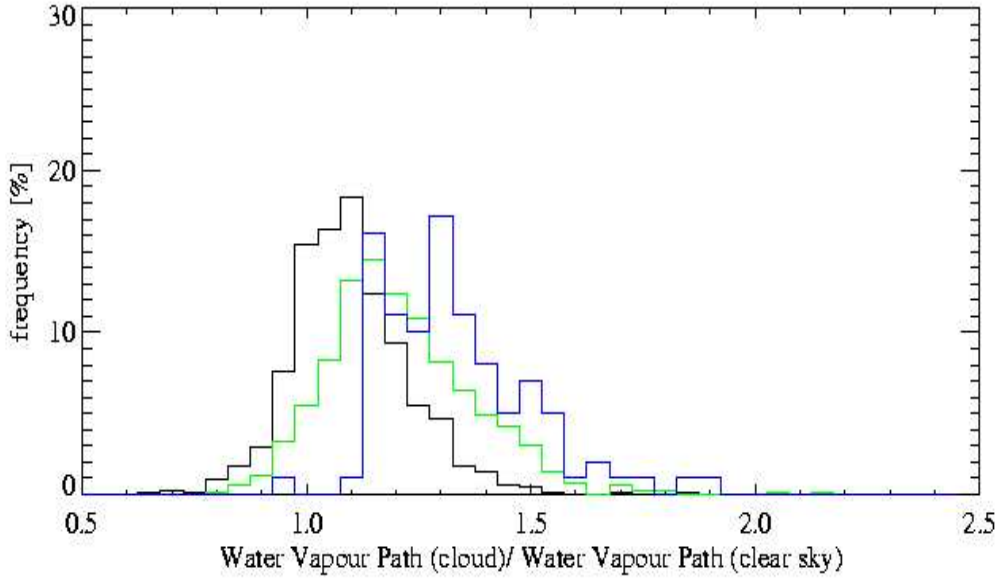

Figure D.32: *Frequency distribution of the excess Water Vapour (WVP(cloudy)/WVP(clear)) vs LWP for clear cases, monthly mean on a 2.5°× 2.5° grid for the South Atlantic. Black: 0-30° South, green: 30-50° South, blue: 50-60° South. The yellow line represents the regression. (September to November 2001).*